PHOTONICS

175 μm
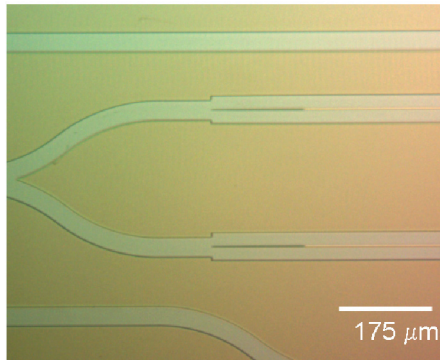
▲ A photograph of the beginning of the second- generation Mach Zehnder interferometer (R. Williams, A. Markina, G.S. Petrich, E.P. Ippen, R.J. Ram, L.A. Kolodziejski, p. 237).

for additional reading...

Organic Photovoltaics with External Antennas

J.K. Mapel, T.D. Heidel, M.A. Baldo

The structures and processes of photosynthesis are evolved, highly efficient, robust, and possess high power density. We attempt to leverage these characteristics by incorporating photosynthetic architectural motifs into organic semiconductor solar cells. We adapt the organization of processes in photosynthesis and introduce a synthetic light harvesting structure into an organic photovoltaic so that it couples light energy to the active device area by near field energy transfer. Light energy absorbed in an artificial antenna layer is transferred to an artificial reaction center in the interior of the solar cell. The energy transfer is of the Förster type, mediated by surface plasmons polaritons. While the introduction of the antenna necessarily adds a step to the energy transduction process, decoupling photon absorption and exciton dissociation can be exploited to increase each separately.

We have experimentally examined the efficiency of energy transfer for this process. We utilize a film of photoluminescent chromophores placed immediately adjacent to an organic solar cell with dual silver electrodes as an antenna layer. We predict and verify that energy transfer can occur in technically relevant device structures with energy transfer efficiencies of approximately 50% and demonstrate this transfer result in increased quantum efficiency.
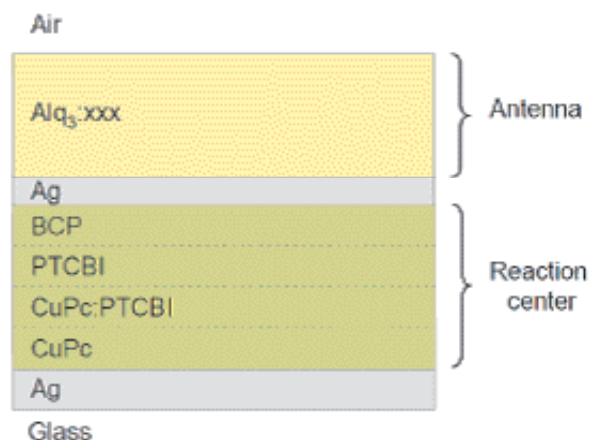
▲ Figure 1: The device structure utilized in these studies is composed of aluminum tris(8-hydroxyquinoline), bathocuproine, copper pthalocyanine, 3,4,9,10-perylenetetracarboxylicbis-benzimidazole, 4-dicyanomethylene-2-methyl-6-(p-dimethylaminostyryl)-4H-pyran, and silver. To tune the emission of the Alq3 antenna it was doped with either CuPc or DCM at 1% weight ratio.
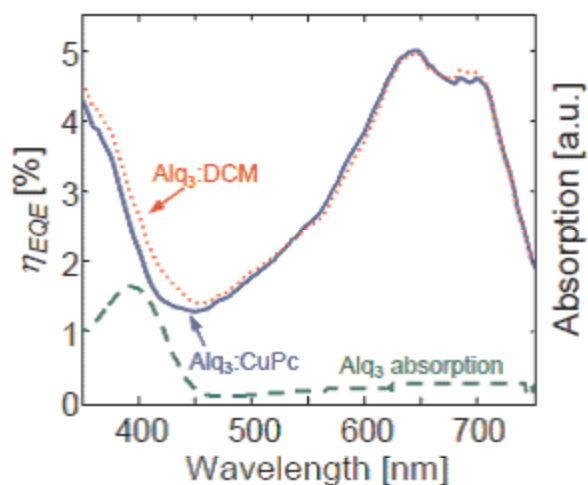
▲ Figure 2: The comparison of devices with functional (dotted line) and nonfunctional (solid line) antennas demonstrate external energy transfer. Devices with functional external Alq3 antenna layers (dotted line) exhibit an increase in external quantum efficiency over the wavelength range where Alq3 absorption occurs (dashed line). The photocurrent spectra are identical outside the spectral range where Alq3 absorbs. Functional antennas employ the laser dye, X = DCM, whereas nonfunctional antennas employ the quencher X = CuPc).

PHOTONICS

211

Optical Models of Organic Photovoltaic Cells

K. Celebi, M.A. Baldo
Sponsorship: DARPA

Common organic photovoltaic devices utilize a direct energy transfer from sunlight to the excitons in the active layers. However, this direct transfer results in a trade-off between the absorption and charge generation by exciton diffusion to the interface [1]. Our group has recently demonstrated a separation of these two processes by absorbing the sunlight in an external antenna and then reemitting the energy in a near-field fashion so that very large exponential fields become possible in the active layers (Figure 1). Calculating the effect of this reemission needs near-field methods since the thicknesses are on the order of the vacuum wavelength of the corresponding emission frequency. To solve this problem, we extend a previously established dyadic Green's functions model [2] to calculate the z-component of the Poynting vector, thus find the spatial absorption of the antenna reemission throughout the multilayer stack (Figure 2). Using these calculations we calculate optimum layer thicknesses for maximum efficiencies. Future work in modeling will concentrate on far-field emission for OLED outcoupling studies and collective dipole behavior.
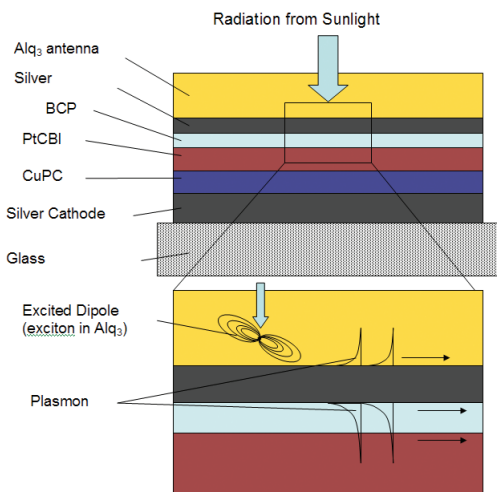
▲ Figure 1: Working principle of the organic PVs with external antennas. Energy is first absorbed by the excitons in the antenna and then these excited excitons transfer their energy to the excitons in the active layers (PtCBI & CuPC) mainly through surface plasmon polariton modes. Structure used is Air/ 800Alq$_3$/ 80Ag/ 100BCP/ 180PtCBI/ 240CuPC/ 400Ag/ Glass (thicknesses are in Angstroms).
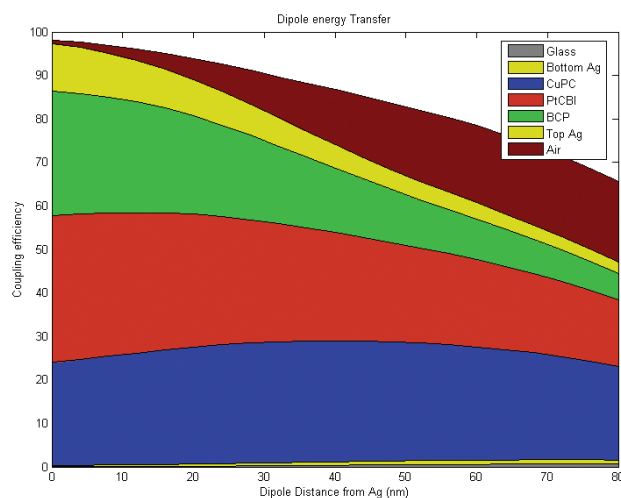
▲ Figure 2: Percentage of power transferred from the excitons in the antenna to different layers in the structure of Figure 1 as a function of exciton distance from the Alq$_3$-Ag interface. White space on the top shows internal damping in the Alq$_3$ molecules. As the exciton distance from silver film increases efficiency decreases due to the reduction in plasmon coupling.

212

REFERENCES

[1] P. Peumans, A. Yakimov, and S.R. Forrest, "Small molecular weight organic thin-film photodetectors and solar cells," *J. of App. Physics*, vol. 93, no. 7, pp. 3693-3723, Apr. 2003.

[2] R.R. Chance, A. Prock, and R. Silbey, "Molecular fluorescence and energy transfer near interfaces," in *Advances in Chemical Physics*, S. A. R. I. Prigogine. NY: Wiley, 1978.

Percolation Model of Charge Transport in Organic Semiconductors

B.N Limketkai, M.A. Baldo
Sponsorship: DuPont-MIT Alliance

In this project, we study charge transport in organic semiconductors using percolation theory. A percolation model was first introduced by Ambegoakar *et al* [1] to explain the hopping conductivity in disordered systems. It was later incorporated in Vissenberg and Matters [2] for an exponential DOS to explain the field-effect mobility in amorphous organic transistors. This percolation model is further employed here, incorporating the effects of an applied electric field to the mobility and current-voltage (IV) characteristics of organic semiconductors. By modifying the percolation model to include the effect of an applied electric field, the temperature and field dependence of mobility and

IV characteristics are found. A universal IV characteristic for organic semiconductors is explained. The Miller-Abrahams expression for charge hopping between exponential trap distributions gives a master equation [3]: $\mathcal{J} = \mathcal{J}_0(V/V_0)^m$, where $\mathcal{J}_0$ and V_0 are constants and $m = 1 + 2\alpha k T_0/(qF + 2\alpha kT)$, where α is the tunneling decay rate, is the power-law slope. Characterization of IV measurements were done with the archetypal organic semiconductor material, tris(8-hydroxyquinoline) aluminum, or Alq_3. Figure 1 shows its molecular structure. To demonstrate the universality of the model, the IV characteristics of a number of Alq_3 devices are overlapped as shown in Figure 2.
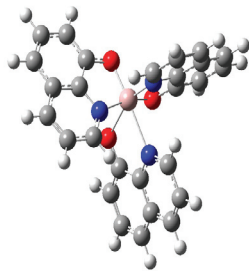
▲ Figure 1: Molecular structure of the archetypal organic semiconductor material, tris(8-hydroxyquinoline) aluminum (Alq_3).
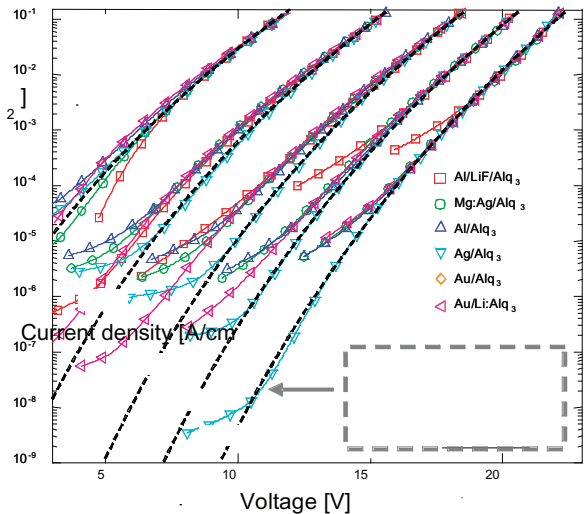
▲ Figure 2: The temperature dependence of the universal IV characteristics of Alq_3 devices. A rigid voltage shift was applied to each IV characteristics to overlap on one another.

PHOTONICS

213

REFERENCES

[1] V. Ambegaokar, B.I. Halperin, and J.S. Langer, "Hopping conductivity in disordered systems," *Physical Review B*, vol. 4. pp. 2612, 1971.

[2] M.C.J.M. Vissenberg and M. Matters, "Theory of the field-effect mobility in amorphous organic transistors," *Physical Review* B, vol. 57. p. 12964, 1998.

[3] B.N. Limketkai and M.A. Baldo, "Charge injection into cathode-doped amorphous organic semiconductors," *Physical Review B*, vol. 71, 085207, 2005.

Integrated Optical-wavelength-dependent Switching and Tuning by Use of Titanium Nitride (TiN) MEMS Technology

S. Takahashi, G.N. Nielson, G. Barbastathis
Sponsorship: DARPA

Ring resonators are integrated optical components that have the capabilities to filter specific bands of wavelength from a broad-band input signal. Although these devices themselves are passive components, by use of evanescent field coupling, the ring resonator can be switched or tuned by electrostaticactuation of a MEMS bridge-type structure above the ring waveguide (Figure 1). This procedure of switching and tuning will allow for a faster speed than thermal tuning and will not induce severe loss, as does carrier injection.

One major issue that must be faced when implementing this concept is the residual stress that the MEMS bridge structure exhibits. Precise vertical positioning of the bridge is crucial for this type of device, and hence the bridge structure must not deflect due to residual stress within the structure. Use of TiN was investigated as the structural material due to its appealing mechanical properties, high electrical conductivity as well as its ability to relax its residual stress by annealing.

The TiN MEMS bridges were fabricated and tested. The MEMS structures were successfully annealed to a flat state, and the actuation voltage of the switch was 90V (Figure 2).

Recently, we have been investigating an architecture which allows for a more flexible design of the device, as well as the capabilities for implementing ultra fast-switching and feedback control of the position of the wafer via capacitance measurement [1]. In this architecture, the ring resonator is fabricated on one wafer and the MEMS structure on another, and the wafers are flip-chip bonded by thermocompression waferbonding with gold.

Wavelength tuning of the ring resonator filter has been numerically simulated by a combination of FEM structural analysis and mode-solver electromagnetic analysis. This analysis showed that tuning of a range of 30 nm with an actuation voltage of 10V was feasible with a silicon oxynitride membrane as the dielectric material.
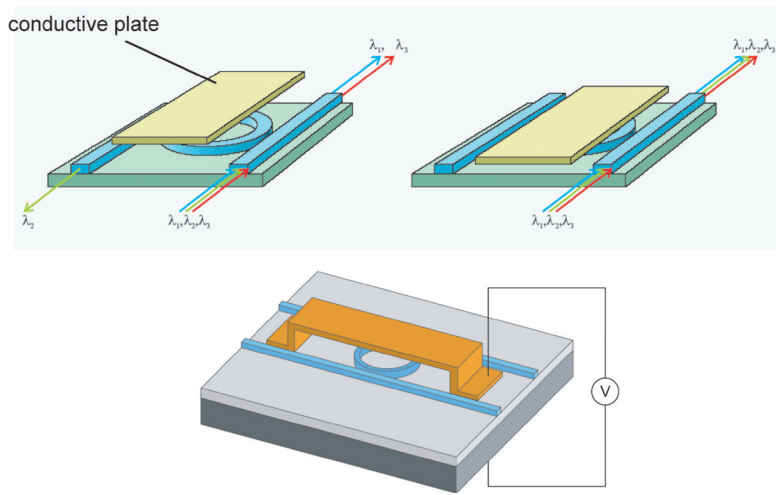
▲ Figure 1: Concept of ring resonator switching via evanescent field coupling (top) and the implemented MEMS-based switching device (bottom). The same concept can be used to tune the resonating wavelength of the ring resonator by using a dielectric material instead of a lossy material, in which case the dropping wavelength on the top left figure will be altered to another wavelength when the membrane is pulled down close to the ring resonator.
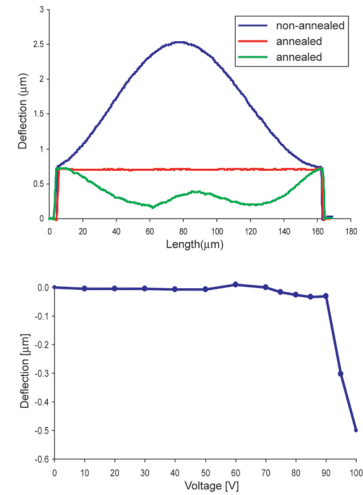
▲ Figure 2: The profile of the TiN MEMS bridge before and after annealing at 500˚C (top), and the voltage vs. deflection curve of the actuated MEMS bridge (bottom).

REFERENCES

[1] G.N. Nielson, "Micro-opto-mechanical switching and tuning for integrated optical systems," Ph.D. thesis, Massachusetts Institute of Technology, Cambridge, 2004.

Four Dimensional Volume Holographic Imaging with Natural Illumination

S.B. Oh, W. Sun, G. Barbastathis
Sponsorship: AFRL, DARPA

Volume holographic imaging is a 3D imaging technique that uses volume holographic lenses. We devised a rainbow volume holographic imaging (RVHI) system, shown in Figure 1. The system projects a rainbow illumination on objects by means of a diffraction grating. Collimated white light is decomposed by a diffraction grating. After passing through a cylindrical lens, the rainbow is focused to the focal plane of a volume holographic lens. All the in-focus points along the x dimension are Bragg- matched; in the y dimension they are also Bragg-matched because of degeneracy. Therefore, the entire rainbow plane is Bragg-matched, resulting in a broad field of view (FOV). When shifted out of focus, each point source in the rainbow becomes Bragg-mismatched due to defocus, much as a narrow-band source at the same wavelength would be[1].

A four-dimensional (3D + spectral) imaging system was devised recently. One unique advantage of this system is that it can be used under natural broadband light illumination on this principle [2]. The imaging process of the 4D imaging system can be understood as a combination of non-invasive optical slicing and spectral analysis. A narrow slit portion (along the y axis) of the object on the focal plane is sampled and its spectrum is laterally imaged on the CCD camera. To cover the entire four-dimensional object space (three spatial dimensions plus one spectral dimension), auxiliary mechanical scanning (rotational mirror as shown in Figure 2) or multiplexing holograms corresponding to different slits are necessary. Also both the 1st order and 0th order diffraction from the volume hologram are measured simultaneously to normalize the brightness of objects.
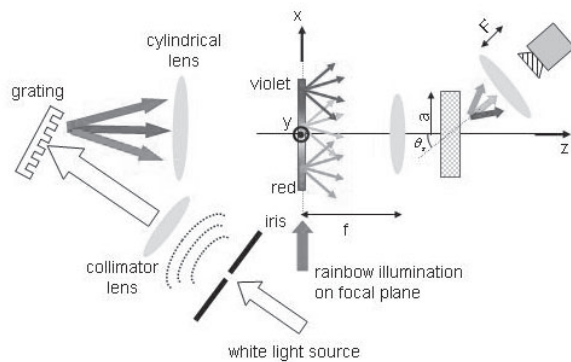
▲ Figure 1: Schematics of rainbow holographic imaging system.
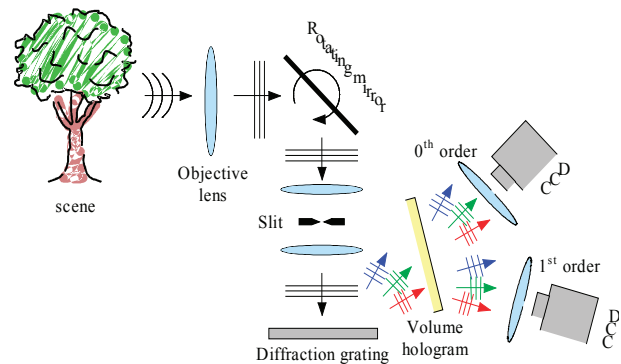
▲ Figure 2: Schematic of the newly devised setup to use volume holographic imaging system under extended white light illumination.

REFERENCES

[1] A. Sinha, W. Sun, T. Shih, and G. Barbastathis, "Volume holographic imaging in transmission geometry," *App. Opt.,* vol. 43, pp. 1533-1551, 2004.

[2] W. Sun, K. Tian and G. Barbastathis, "Hyper-spectral imaging with volume holographic lenses," in *Proc. CFP2 Conference on Laser and Electro-Optics (CLEO),* Baltimore, MD, 2005.

Guided-Wave Devices for Video Display Applications

D. Smalley, V.M. Bove, Jr., Q. Smithwick
Sponsorship: CELab, Digital Life, and Things That Think research consortia, MIT Media Lab

We are developing a guided-wave optical modulator[1-2] with 1 Ghz composite bandwidth surface acoustic wave (SAW) transducer arrays for use in video display. This device is designed to diffract light both vertically and horizontally by creating surface acoustic waves that interact with light trapped in waveguides on the surface of a lithium niobate substrate. To fabricate this modulator, we first mask a wafer of Z-cut lithium niobate with SiO_2 through a PECVD process and then we immerse it in heated benzoic acid to create single polarization waveguides. Finally, we pattern aluminum transducers onto the waveguides by contact lithography employing a negative resist lift-off technique.

The goal of this work is to enable the inexpensive manufacturing of Scophony-architecture video displays [3] (both 2D and holographic video [4-5]) without the need for the horizontal scanning mirrors that typically limit the scalability of this technology.
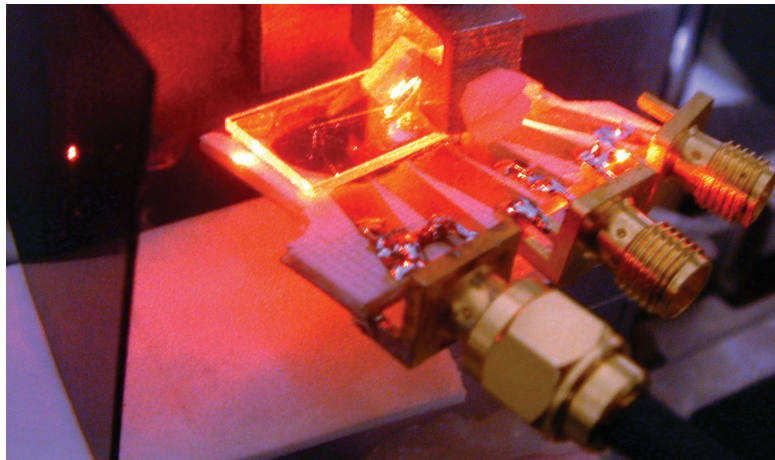
▲ Figure 1: Prototype 2-D guided-wave acousto-optic device for video display applications.

REFERENCES

[1] C.S. Tsai, Q. Li, and C.L. Chang, "Guided-wave two-dimensional acousto-optic scanner using proton-exchanged lithium niobate waveguide," *Fiber and Integrated Optics,* vol. 17, pp. 157-166, 1998.

[2] D. Smalley, "Integrated-optic holovideo," Master's thesis, MIT, Cambridge MA, 2006.

[3] H.W. Lee, "The Scophony television receiver," *Nature,* vol. 142, pp. 59-62, July 9, 1938.

[4] P. St.-Hilaire, S.A. Benton, M. Lucente, J.D. Sutter, and W.J. Plesniak, "Advances in holographic video," in S.A. Benton, ed., *SPIE Proc. Vol. #1914: Practical Holography VII,* 1993, pp. 188-196.

[5] W. Plesniak, M. Halle, V.M. Bove, Jr., J. Barabas, and R. Pappu, "Reconfigurable Image Projection (RIP) holograms," *Optical Engineering,* to be published.

Energy Transfer from an Organic Phosphorescent Thin Film to a Monolayer of Quantum Dots

P.O. Anikeeva, C F. Madigan, S.A. Coe-Sullivan, J.S. Steckel, M.G. Bawendi, V. Bulović
Sponsorship: ISN, NSF Materials Research Science and Engineering Center at MIT, PECASE

Over the past several years the optical and electronic properties of colloidaly synthesized nanocrystals, or quantum dots (QDs), of CdSe have been extensively studied, with the aim of using QD films in solid-state opto-electronic devices. Efficient exciton generation in CdSe QDs suggests use of nanocrystal composite films in photovoltaic cells, while high luminescence quantum yields and tunability of QD emission wavelengths over the entire visible spectrum suggests QD film use in light-emitting devices (LEDs). These developments are a consequence of advances in colloidal QD synthesis that allow for increased control over the shape, size, and emission wavelength of nanocrystals and the development of methods for forming QD thin films of controlled structure and composition. We utilize these advances in the present study to demonstrate triplet exciton energy transfer (ET) from a thin film of phosphorescent molecules to a monolayer of CdSe/ZnS core/shell QDs (Figure 1). Triplet exciton harvesting and transfer to an efficient lumophore has been previously used in advancing organic light emitting device (OLED) technology and has the potential to similarly benefit the emerging field of quantum-dot-LEDs.

The efficient energy transfer is facilitated by the spectral overlap of the organic phosphor fac tris(2-phenylpyridine) iridium (Ir(ppy)$_3$) luminescence and QD absorption spectra. In time-resolved photoluminescence (PL) measurements, the energy transfer is manifested as elongation of the QD PL time constant from 40 ns to 400 ns (Figure 2) and a concomitant 55 % increase of time-integrated QD PL intensity. Numerical analysis supports the conclusion that the observed PL dynamics are dominated by exciton diffusion within the Ir(ppy)$_3$ film to the QD layer, energy transfer from Ir(ppy)$_3$ to QD film, and subsequent QD luminescence [1].
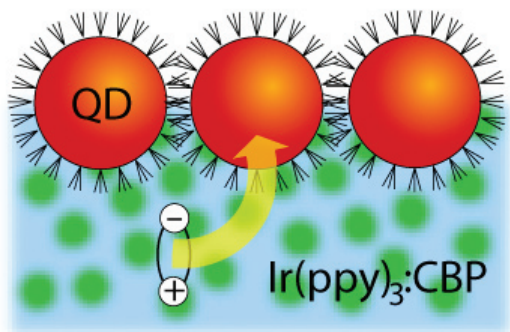
▲ Figure 1: Schematic diagram of the energy transfer form an organic film doped with a phosphorescent donor to a monolayer of colloidal CdSe/ZnS core-shell QDs.
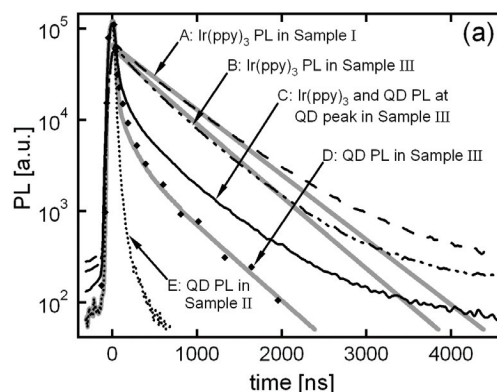
▲ Figure 2: Time resolved PL measurements for samples I, II, and III, which respectively correspond to Ir(ppy)$_3$ film on glass, QD layer on glass, and QD layer on Ir(ppy)$_3$ film on glass . The black lines and dots represent the experimental measurements, and the thick grey lines represent numerical fits using the proposed diffusion model. Data set A represents Ir(ppy)$_3$ PL decay in purely organic sample, data set B represents Ir(ppy)$_3$ PL decay in contact with QDs, data set C represents QD and Ir(ppy)$_3$ PL decay in contact with each other at QD PL peak position, data set D represents QD dynamics in contact with Ir(ppy)$_3$, data set E represents QD dynamics in purely QD sample.

REFERENCES

[1]   P.O. Anikeeva, C.F. Madigan, S.A. Coe-Sullivan, J.S. Steckel, M.G. Bawendi,and V. Bulović, " Photoluminescence of CdSe/ZnS core/shell quantum dots enhanced by energy transfer from a phosphorescent donor," *Chem. Phys. Lett.,* vol. 424, no. 1-3, pp. 120-125, June 2006.

White Light QD-LEDs

P.O. Anikeeva, J.E. Halpert, M.G. Bawendi, V. Bulović

We are developing white-light emitting quantum dot LEDs (QD-LEDs) for use as planar white-light sources in the full-color active-matrix displays with color filters and in future solid-state lighting. Our white QD-LEDs consist of organic charge transport layers with a QD monolayer sandwiched between them. This device architecture enables independent processing of the charge transport layers and the emissive layer. The independent processing of QDs is a result of the recent development of the QD printing technique, which allows for the solvent–free deposition of QD monolayers onto various organic materials [1]. By mixing different amounts of high quantum-yield colloidal core/shell QDs (red CdSe/ZnS, green ZnCdSe/ZnS, blue CdS/ZnS), we demonstrate different QD-LED colors. Figure 1a shows electroluminescence of the white QD-LED with the CIE (Commission International de l'Eclairage) coordinates of (0.42, 0.41). Figure 1b and inset of Figure 2 also show that CIE coordinates vary only slightly under the different applied bias and different operation time [2].
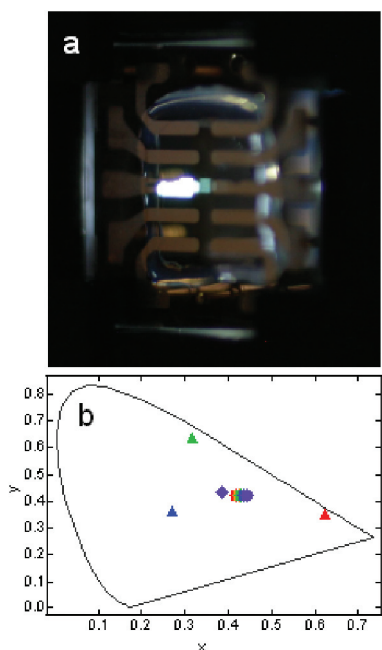
▲ Figure 1: a) Photograph of a white QD-LED operated at 10 V of applied bias. b) CIE coordinates of QD-LEDs: red (red triangle), green (green triangle), blue (blue triangle), and white (purple diamond at 12 V. Change of color with operation lifetime is shown with progression from red circle to purple circle for a QD-LED operated at 9 V.
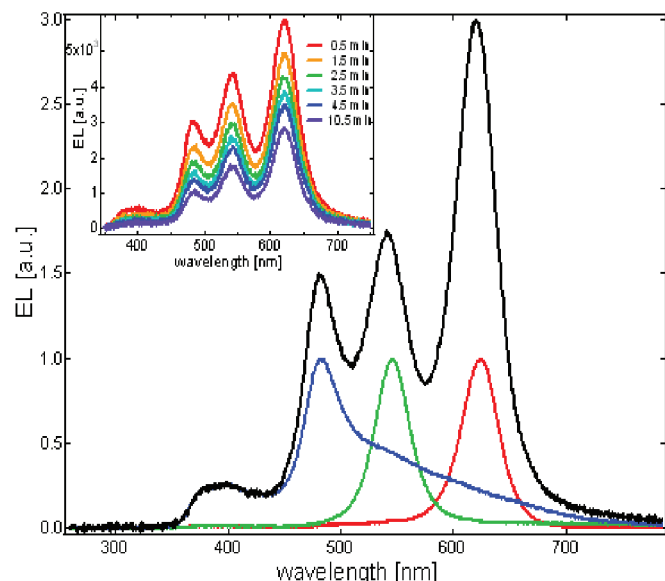
▲ Figure 2: Electroluminescence of the blue (blue line), green (green line), red (red line), and white (black line) QD-LEDs shown not to scale to demonstrate the presence of the spectral signatures of all three QD colors in the white device spectrum. Inset: We observe slight change of the spectral shape of the white QD-LED with operation time.

REFERENCES

[1] S.A. Coe-Sullivan, "Hybrid organic/quantum dot thin film structures and devices," Ph.D thesis, Massachusetts Institute of Technology, Cambridge, 2005.

[2] P.O. Anikeeva, J.E. Halpert, M.G. Bawendi, and V. Bulović, unpublished results.

Organic Optoelectronic Devices Printed by the Molecular Jet Printer

J. Chen, V. Leblanc, M.A. Baldo, M.A. Schmidt, V. Bulović
Sponsorship: Hewlett-Packard

Using a micro-fabricated silicon printhead, we developed a novel printing technique, molecular jet printing (MoJet) [1-2] that allows direct patterning of small molecular weight organics and metals by additive deposition at high resolution. Today's dominant method for patterning vacuum-deposited semiconducting molecular organics uses a thin metal stencil as a shadow mask through which material evaporates. Once the metal stencil is fabricated, it cannot be reconfigured to define arbitrary patterns or be scaled up with substrate size. In contrast, the MoJet printing technique utilizes a silicon printhead that integrates a moving micro-shutter with a micro-aperture. The shutter can be opened or closed with a DC control signal. Evaporated organic molecules can either pass through the aperture to reach the substrate when no bias is applied or be obstructed by the shutter when the control signal is above 30 V DC. This reconfigurable printhead together with a moving stage allows arbitrary patterning capability and scalability of the MoJet printer to larger substrate sizes.

We demonstrate that active organic devices such as organic LEDs and organic FETs (see graphics below) can be fabricated directly using the MoJet printer. The MoJet printing is a solvent-free process (in contrast to ink-jet printing) that combines the high quality of thermally evaporated thin films with the high precision and scalability enabled by MEMS technology. The MoJet printed organic electronic devices have the same performance characteristics as those defined by the shadow-mask patterning method, but the size of the substrate plate can now be expanded beyond GEN 2/3. As such, the MoJet printer surpasses the capability of the metal-stencil shadow mask and has the potential to become the next generation patterning tool for making organic optoelectronic devices.

1. Mg:Ag alloy cathod (150nm)
2. TAZ (ETL) (30 nm)
3. Printed alq3 array (EL) (12nm)
4. TPD (HTL) (30 nm)
5. PEDOT:PSS (HIL)
6. ITO anode
7. Glass substrate

50µm
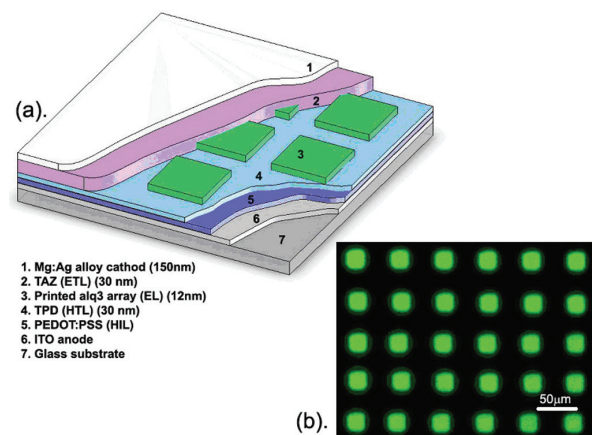
▲ Figure 1: (a) Layer structure of printed OLED array. The green electroluminescent layer (EL) is directly printed with the MoJet printer. (b) EL micrograph of active OLED array at 7.5V applied voltage. The image is taken through a 470-nm low-pass filter to reveal that green pixel patterned by the MoJet. The pixel size is 30 µm, equivalent to 800 dpi resolution.

1. Printed silver contact as source (40nm)
2. Printed silver contact as drain (40nm)
3. Printed pentacene channel (30nm)
4. Silicon dioxide dielectric layer (200nm)
5. Silicon substrate as gate

50µm
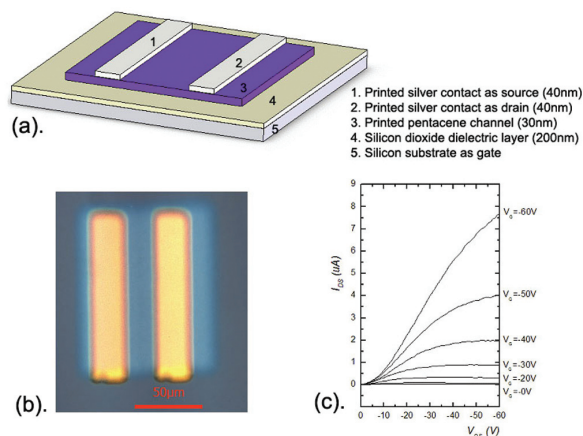
▲ Figure 2: (a) Structure of the printed Pentacene transistor. Pentacene layer is printed down first and silver contacts are printed sequentially. (b) Micrograph of a single-printed OFET on silicon oxide. (c) The I-V characteristics of one of the transistors. The gate voltage Vg is varied from 0 to –60V in 10V steps.

REFERENCES

[1] V. Leblanc, S.H. Kang, J. Chen, P.J. Benning, M.A. Baldo, V. Bulović, and M.A. Schmidt, "Micromachined printheads for the patterning of organic materials and metals," *Proc. of Transducers 2005*, Seoul, pp. 1429-1432.

[2] J. Chen, V. Leblanc, S.-H. Kang, M.A. Baldo, P.J. Benning, V. Bulović, and M.A. Schmidt, "Direct patterning of organics and metals using a micro-machined printhead," *Proc. MRS Spring 2005*, H1.8

Charge Dynamics in Organic Heterojunction Lateral Photoconductors

J. Ho, V. Bulović

The purpose of this project is to develop solid-state, organic device structures capable of efficiently converting analyte detection into an attenuation in electrical signal. The main advantage to using organic materials is that they are synthetically flexible and can be tailored to respond to specific analytes. Our proposed device structure is a heterostructure consisting of an optically active, chemosensing layer and a charge-transport layer arranged in a lateral photoconductor-style device (Figure 1A). The advantages to physically separating the sensing and transport functions in chemical sensors include: 1) the ability to optimize the transduction of luminescence to device current, and 2) the development of a reusable device platform for a variety of chemosensing applications.

In addition to developing a novel device platform for chemical sensing, we are using this novel structure to study charge transport and exciton dynamics in organic thin films (Figure 1B). The devices consist of a series of gold interdigitated fingers (W x L = 1500 μm x 4 μm) spaced 10 μm apart (Figure 1A). The gold electrodes are photolithographically defined on glass before the organic layers are thermally evaporated. Locked-in measurements of the photocurrent spectra suggest external quantum efficiencies ranging from 10-15%. Initial experiments indicate an enhancement in photoresponse of the heterostructure devices over devices made from bulk films of both materials (Figure 2).
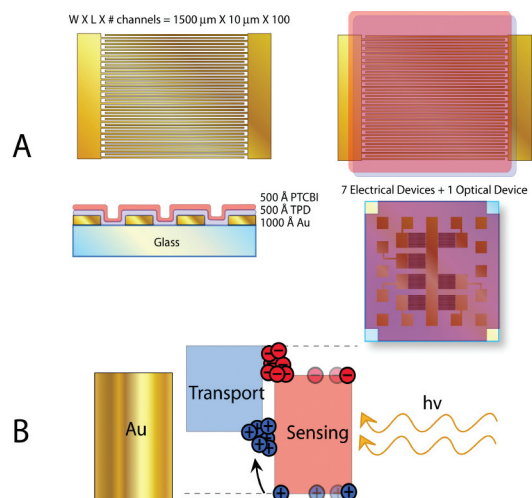
▲ Figure 1: A) Schematic drawings of lateral photo conductor devices. Clockwise from upper left are photolithographically defined gold electrodes, electrodes with evaporated organic thin films, cross-section view, and top view of actual substrate. B) Mock band diagram of device showing exciton generation, exciton diffusion, and charge carrier build-up at the heterostructure interface.
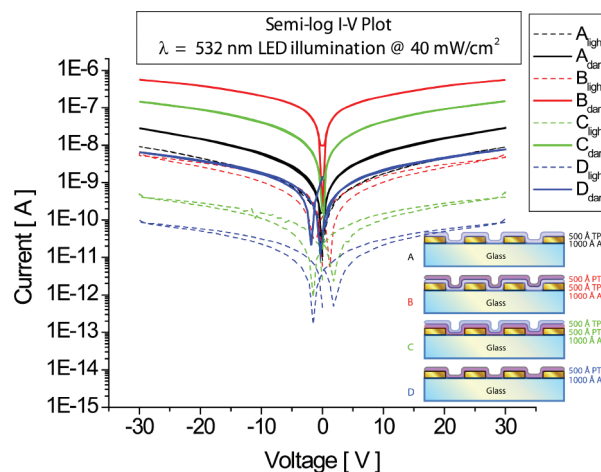
▲ Figure 2: Semi-log current-voltage characteristics of bulk and heterostructure lateral photoconductor devices. Dotted lines represent I-V curves in dark. Solid lines represent I-V curves under LED illumination centered at λ = 532 nm. Inset: Cross-sections of tested devices. Note the different photoresponse curves between the bulk and heterostructure devices.

Packing of Quantum Dot Monolayers

E. Howe, V. Bulović
Sponsorship: MARCO MSD

We developed a kinetic model for assembly of ordered quantum-dot (QD) monolayers on a 2-dimensional surface that reproduces experimental observations for a variety of QD size distributions (of Gaussian size profile). Such QD monolayers have already been utilized in a number of thin-film applications, QD-LEDs, and QD-photodetectors. However, methods of fabricating QD films are still being developed and our work focuses on developing a numerical tool to investigate methods for improving the quality of these films.

To numerically assemble a QD monolayer, we model the QDs as spheres that move on the surface with no friction but with random thermal motion added at each time-step. We apply a van der Waals attraction between QDs and hard-wall repulsion at the QD radius. When two QDs collide, their interaction is partially inelastic based on a model parameter. These conditions allow for a range of behavior encompassing many interesting phenomena. We find that a mono-disperse size distribution of QDs forms hexagonally close-packed aggregates, and the packing and aggregate stability of the QD monolayer degrades dramatically as the standard deviation of the size distribution is increased. In experimental studies [1], the instability of QD monolayers has been observed to occur for standard deviations of greater than 10% in QD diameter. We were able to reproduce these findings in our simulations (Figure 1). We have further shown that confining the same QD distributions inside a 1-dimensional hard boundary with a width of a few QD diameters can counteract this instability.
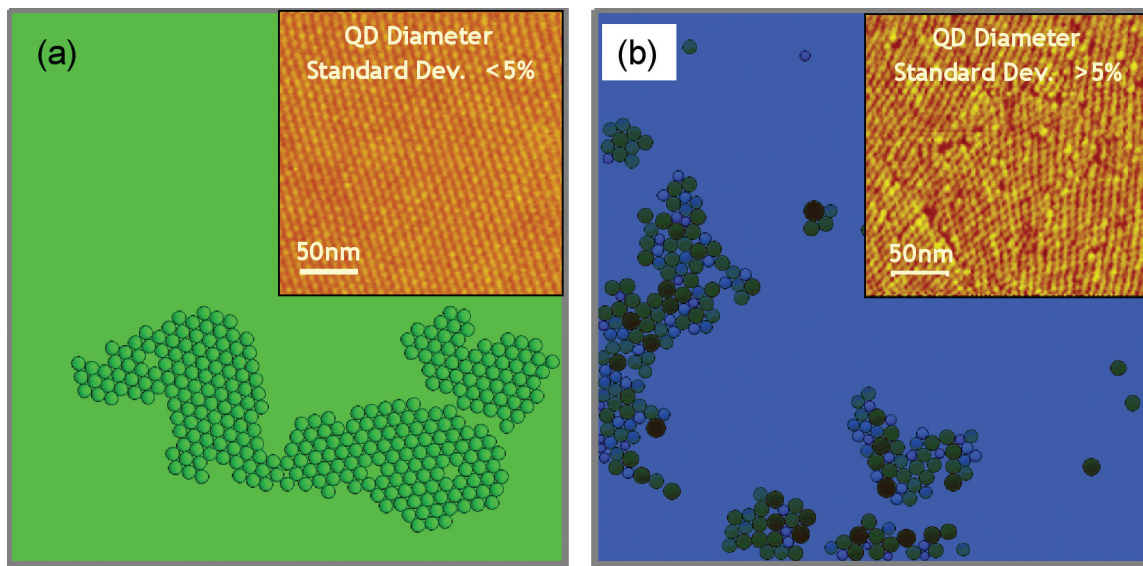
▲ Figure 1: (a) Results of simulation of packing for 300 QDs of equal size. The inset is an AFM image [1] of a monolayer of QDs with less than 5% standard deviation in diameters. In our simulation we observe the same hexagonal close-packed arrangement of QDs and stability of aggregates that allows for good monolayer formation. (b) Results of simulation for packing 300 QDs with a 15% standard deviation in diameters. The inset is an AFM image for the same method of preparation as (a) but with QDs having a greater than 5% standard deviation in diameters. For these large size distributions, our simulated dots could no longer form hexagonally close-packed arrays. In addition, aggregates readily broke up as dots were less well-bound.

REFERENCES

[1] S. Coe-Sullivan, J.S. Steckel, W.-K. Woo, M.G. Bawendi, V. Bulović, "Large-area ordered quantum-dot monolayers via phase separation during spin-casting," *Advanced Functional Materials,* vol. 15, no. 7, pp. 1117-1124, 2005.

Energy Disorder and Device Performance in Organic Electronics

C.F. Madigan, V. Bulović
Sponsorship: MARCO MSD, NDSEG Fellowship

Presently many organic electronic devices employ amorphous materials, and it is well known that the molecular energy levels in such materials are subject to disorder arising from variations in local intermolecular interactions. The movement of molecular charge carriers and excitons through the constituent materials largely controls the performance of such devices, and it has been well established that energy disorder strongly influences charge carrier and exciton motion. Though accurate analytic treatments remain elusive, Monte Carlo (MC) simulations of charge carrier and exciton hopping between molecular sites subject to energy disorder have proven an effective tool for analyzing charge carrier and exciton motion in such materials [1]. Combining MC simulations with accurate models of energy disorder should make it possible to perform calculations of device behavior in realistic structures with relatively few theoretical model assumptions. This project addresses: (1) the theoretical calculation of energy disorder in amorphous organic materials; and (2) the application of MC simulations to realistic device structures and operating conditions. We have performed exact calculations of charge carrier and exciton energy disorder arising from electrostatic interactions between structurally disordered, polarizible molecular charge distributions (see Figure 1). These calculations differ from those in the literature because the molecular polarizibility is explicitly included in the calculation, avoiding the need to employ dielectric continuum approximations (DCAs). It is found that the widely used DCAs are inaccurate, and we presently are developing improved expressions for relating the magnitude of the disorder to the material properties (principally, the molecular dipole moment, the molecular density, and the dielectric constant). We have also developed an MC simulator of charge carrier and exciton motion in energetically disordered molecular materials capable of treating realistic device geometries (e.g., multilayer stacks and electrical contacts). Because organic electronic devices often operate at high carrier concentrations, we have also included basic charge-carrier interactions to treat the effects of carrier concentration on charge transport; these effects have not been previously investigated using the MC simulation technique. We are presently performing calculations of carrier mobilities as a function of field and carrier concentration (see Figure 2) for comparison with existing approximate analytic approaches. These studies support future simulations of real device structures for a rigorous comparison of experimental device performance and theory.
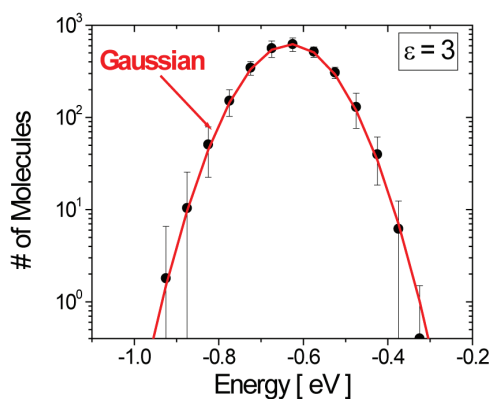
▲ Figure 1: Calculation of charge carrier energy disorder (in the form of the histogram of energies for a large collection of interacting molecules) for a structurally random molecular solid, composed of molecules having a dipole moment of 2 Debye, a molecule density of 1e21 cm^{-3}, and a dielectric constant, Σ, of 3. The black symbols denote the raw data, and the red line indicates a fit using a Gaussian function.
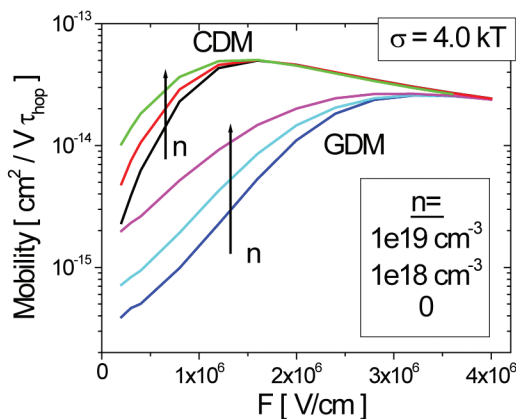
▲ Figure 2: Calculations of charge-carrier mobility as a function of field, F, and carrier concentration, n, in an energetically disordered molecular organic material. In these calculations, the standard deviation of the energy disorder, $\int$, is 4.0 kT, where kT is the thermal energy. Calculations for two different energy disorder models, the Gaussian disorder model (GDM) and the correlated disorder model (CDM) are shown.

REFERENCES

[1] C.F. Madigan and V. Bulovic, "Modeling of exciton diffusion in amorphous organic thin films," *Phys. Rev. Lett.*, vol. 96, pp. 046404:1-4, Feb. 2006.

Strong Coupling of Light and Matter in a Microcavity LED

J.R. Tischler, M.S. Bradley, V. Bulović
Sponsorship: DARPA Optocenter, NDSEG, NSF-MRSEC

We have demonstrated the first microcavity light emitting device (LED) in which light emission is produced from strongly coupled states of light and matter by electrical excitation [1]. Applications of strong coupling in atomic and semiconductor systems have led to one-atom zero threshold lasers, high gain polariton parametric amplifiers, and predictions that strong coupling may play a key role in future quantum information processors. These previous experiments have all relied on optical pumping. We achieve strong coupling in the microcavity LED by electrically exciting a 6±1 nm thick film of J-aggregated dye that we embedded into a resonant cavity organic LED (RC-OLED) structure. Specifically, the film of J-aggregated dye is composed of the anionic cyanine dye TDBC. which is electrostatically adsorbed to the cationic polyelectrolyte PDAC (poly diallyldimethylammonium chloride). These films contain a high density of J-aggregated TDBC and therefore have very large peak absorption constant ($\alpha \sim 1.0 \times 10^6$ cm^{-1}). We achieved a coupling strength (Rabi-splitting) of $h\Omega = 265 \pm 15$ meV with 6 nm thick films of active material and even larger coupling strengths should be achievable with thicker films. Figure 1 shows that the device exhibits angular dispersion in the reflectivity and electroluminescence measurements that is characteristic of the strong coupling limit.
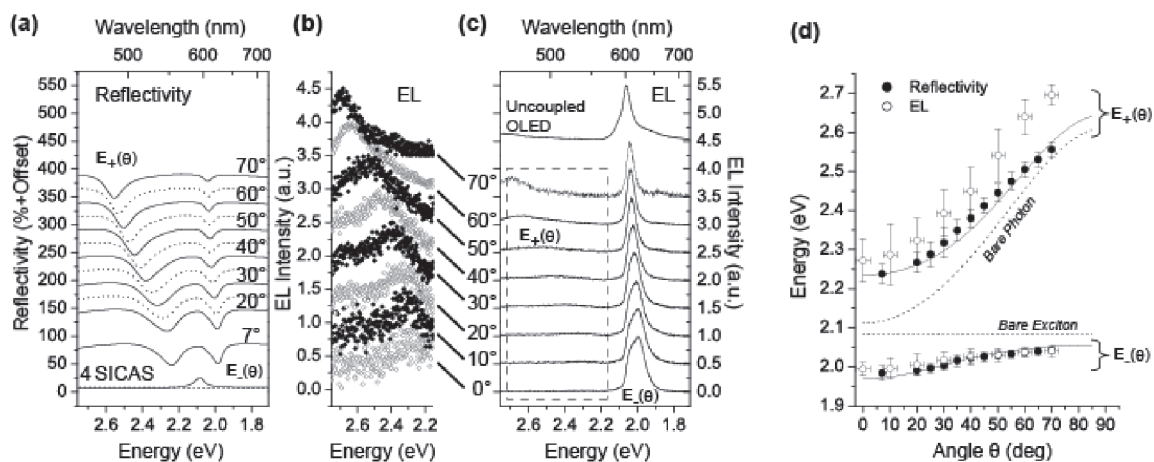
▲ Figure 1: Angularly resolved polariton electroluminescence, reflectivity, and dispersion relations for near- resonantly tuned polariton RC-OLED. (a) TE polarized reflectivity. Data of successive measurements are offset by 50 percentage points. The reflectivity at θ = 7° of a 6 nm thick PDAC/TDBC film (4 SICAS), is shown for comparison. (b) Expanded view of higher energy portion of the EL spectra, normalized to emission of the higher energy polariton peak, $E_+(\theta)$, in the λ = 450 nm to λ = 575 nm range. (c) The EL spectra normalized to lower energy polariton peak, $E_-(\theta)$. The EL spectrum at θ = 0° of an uncoupled OLED is shown for comparison. (d) Polariton angular dispersion relation for RC-OLED of parts (a-c) with $E_{ph}(\theta = 0°) = 2.11$ eV. The fit is generated from reflectivity data in (a) using the two-state model of Eq. 1 with the coupling interaction, $h\Omega = 265$ meV.

REFERENCES

[1] J.R. Tischler, M.S. Bradley, V. Bulović, J.H. Song, and A. Nurmikko, "Strong coupling in a microcavity LED," *Phys. Rev. Lett.,* vol. 95, no. 3. pp. 034061-034064, July 2005.

Critically Coupled Resonators in Vertical Geometry, Capable of Absorbing Nearly 100% of Incident Light in a 5 nm thick Absorber Layer

J.R. Tischler, M.S. Bradley, V. Bulović
Sponsorship: DARPA Optocenter, NDSEG, NSF-MRSEC

When light of wavelength $\lambda_c = 584$ nm is incident on the critically coupled resonator (CCR) structure illustrated in Figure 1a from the absorbing layer side of the device, the measured reflectance is R = 2%, as shown in Figure 1b [1]. In contrast, for the DBR with spacer but without the absorbing layer, the reflectivity at $\lambda_c = 584$ nm exceeds 95%, showing the dramatic change in reflectance due to critical coupling. For the same CCR, the transmittance at λ_c is T = 1%. Consequently, 97% of the incident light is absorbed within the 5.1 ± 0.5 nm thick absorber layer, yielding a maximum effective absorption coefficient of $\alpha_{eff} = 6.9 \times 10^6$ cm$_{-1}$. We developed a generalized model of the CCR phenomenon and have shown through simulation that critical coupling is achievable with a variety of material sets, providing several general conditions are satisfied. Among non-epitaxially grown materials, we can envision building CCR's with organic polymers that are used in biological assays and chemical sensors, with molecular materials that are used in photodetectors and xerographic photoresistors, and in the emerging uses of colloidally grown inorganic nanocrystal quantum-dots (QDs). Application of the CCR phenomenon can also facilitate development of single-photon optics where it is desirable to absorb a photon with 100% probability in the thinnest possible films and of colloidally grown semiconductor saturable absorber mirrors for ultra-fast optical modulators.
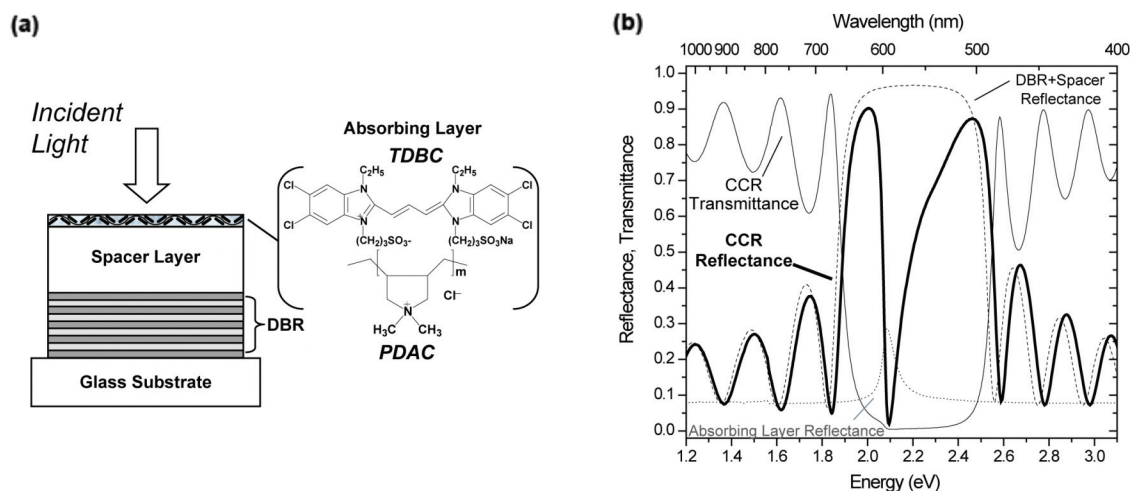
▲ Figure 1: a) Critically coupled resonator (CCR) structure. The device consists of a dielectric Bragg reflector (DBR), a transparent spacer layer, and a layer of J-aggregate cyanine dye. The J-aggregate layer consists of the cationic polyelectrolyte, PDAC, and the anionic cyanine dye, TDBC. Reflection and transmission measurements are made with light incident from the J-aggregate side of the device. b) Reflectance and transmittance data for the CCR with spacer layer thickness of 90 ± 1 nm, along with reflectance data for the neat PDAC/TDBC film and for the dielectric stack consisting of DBR with spacer layer. At λ_c=584 nm, the CCR absorbs 97% of incident light.

REFERENCES

[1]   J.R. Tischler, M.S. Bradley, and V. Bulović, "Critically coupled resonators in vertical geometry using a planar mirror and a 5 nm thick absorbing film," *Opt. Lett.*, vol. 31, pp. 2045-2047, 2006

Resonant Cavity Quantum Dot LEDs

V. Wood, J.R. Tischler, V. Bulović
Sponsorship: NSF, PECASE

Quantum dot LEDs (QD-LEDs), which capitalize on the excellent color saturation and high photoluminescence efficiencies offered by quantum dots, promise to be part of future generations of display technologies [1]. The goal of our project is to integrate the already developed technology of the QD-LED into a resonant cavity (RC) and thereby achieve enhanced, directed electroluminescence (EL) that can be of use in fields as diverse as optical communications, spectroscopy, and environmental and industrial sensing.

The RC structure we are currently investigating (Figure 1) consists of a standard QD-LED [1] grown on top of a distributed Bragg reflector (DBR). A DBR is a highly reflective mirror made of $\lambda/4$ layers of alternating high and low indices of refraction. With a reflectivity of more than 98% in the wavelength region of interest, the DBR serves as one of the cavity mirrors. The other cavity mirror is the Ag doped Mg electrode of the QD-LED. With this structure, we have achieved narrowed emission, which is evident when comparing EL spectra and images of the QD-LED and the RC QD-LED (Figure 2). The QD-LED appears orange because our eyes sense the red light of the QDs as well as the shorter wavelength emission from the organics. In contrast, the RC QD-LED exhibits effectively monochromatic red light. The plot of peak emission intensity at different angles (Figure 2) shows an emission cone of less than twenty degrees. If the path-length of the cavity does not match the QD emission wavelength, EL from the RC QD-LED is off-normal. We are currently working to understand the emission enhancement capability of our RC QD-LED.
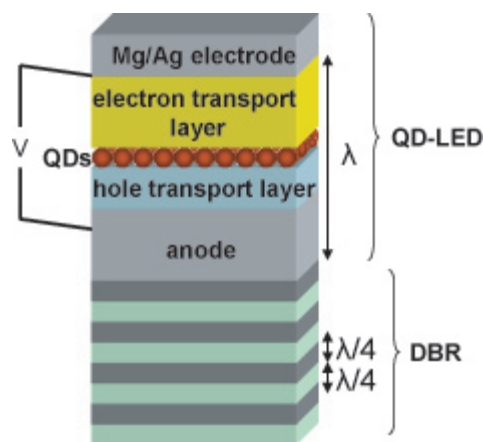
▲ Figure 1: Schematic of RC QD-LED.
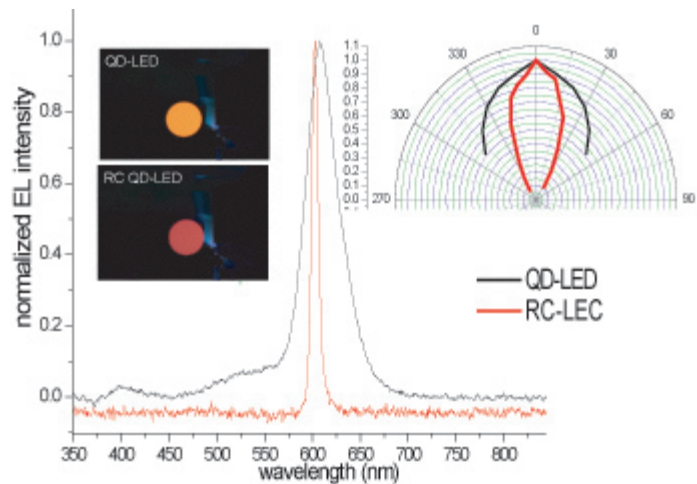
▲ Figure 2: Comparison of EL spectra, images, and angular emission profiles of RC QD-LED and QD-LED. The RC QD-LED exhibits marked narrowing.

REFERENCES

[1] S. Coe, W.K. Woo, M. Bawendi, and V. Bulović, "Electroluminescence from single monolayers of nanocrystals in molecular organic devices," *Nature*, vol. 420, no. 6917, pp. 800-803, Dec. 2002.

Patterning Micron-Sized Features of Quantum Dots and Metal Electrodes

J. Yu, J. Chen, V. Bulović
Sponsorship: ISN, NSF Materials Research Science and Engineering Center at MIT, PECASE

Organic LEDs (OLED) and quantum-dot LEDs (QD-LED) are promising technologies for the emissive element in flat panel displays. However, organic material in these devices is sensitive to solvent exposure and creates processing challenges in patterning a pixelated display. This project aims to develop novel fabrication processes for OLED and QD-LED displays.

In QD-LEDs, quantum dots can be patterned by spin-casting a monolayer onto a relief poly(dimethylsiloxane) (PDMS) stamp and then transferring the pattern onto an organic substrate [1]. However, the spin-cast process requires significant use of material. An alternative solution is to directly pattern the dots using thermal inkjet pico-fluidic drop dispensing system (TIPS) provided by Hewlett-Packard (Figure 1a). A process for formation of patterned monolayer using this technique is currently being developed.

Patterning of electrodes in OLED or QD-LED displays presently is done primarily by shadow masking, which is limited in resolution; or cold-welding, which requires high pressures, additional protection layers, use of gold electrode, or subsequent dry etching steps [2-3]. Recently transfer printing has been demonstrated with PDMS on various materials [4]. We are investigating subtractive pattering of silver or silver-magnesium electrodes with untreated PDMS stamp. We demonstrated 25 micron-sized features with good yield on 20 nm thick silver-magnesium films (Figure 1b). This PDMS lift-off technique applied on an OLED electrode made of 50 nm silver film on top of 50 nm silver-magnesium yields OLEDs with the same quantum efficiency and current voltage characteristics to OLEDs defined by shadow masking (Figure 2).
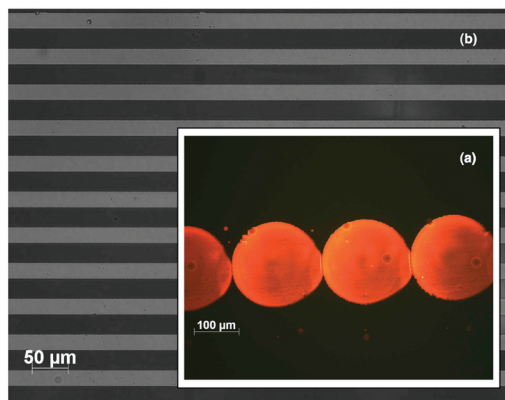
▲ Figure 1: a) Patterned quantum dot features using TIPs system. b) PDMS lift-off of 20-nm-thick silver-magnesium electrodes.
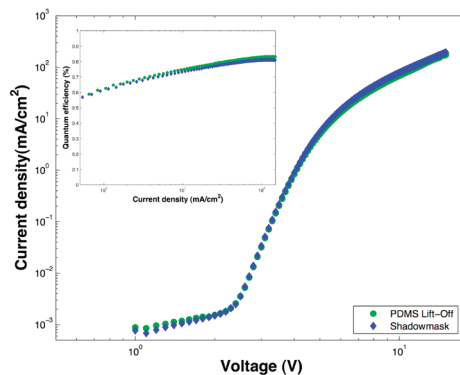
▲ Figure 2: Comparison of current voltage characteristics for shadow-masked and PDMS lift-off electrode for typical ITO, PEDOT, 50-nm Alq$_3$, 50-nm TPD, 50-nm Mg:Ag, 50-nm Ag OLED. Inset: Quantum efficiency vs. current characteristics.

REFERENCES

[1] L. Kim, "Deposition of colloidal quantum dots by microcontact printing for LED display technology," Master's thesis, Massachusetts Institute of Technology, Cambridge, 2006.

[2] C. Kim, P. Burrows, and S. Forrest, "Micropatterning of organic electronic devices by cold-welding," *Science*, vol. 288, pp. 831-833, May 2000.

[3] C. Kim and S. Forrest, "Fabrication of organic light-emitting devices by low-pressure cold-welding," *Advanced Materials*, vol. 15, no. 6, pp. 541-545, Mar. 2003.

[4] M. Meitl, Z. Zhu, V. Kumar, K. Lee, X. Feng, Y. Huang, I. Adesida, R. Nuzzo, and J. Rogers, "Transfer printing by kinetic control of adhesion to an elastomeric stamp" Nature Material, vol. 5, pp. 33-38, Jan 2006.

SiO$_x$N$_y$ Waveguides on Si and Optical Coupling to Co-Axial RM³ Integrated Devices

E.R. Barkley, J.J. Rumpler, J.M. Perkins, S. Famini, C.G. Fonstad, Jr.
Sponsorship: DARPA

We present research in progress on the design, fabrication, and characterization of rectangular, buried-channel silicon oxynitride waveguides. We are currently pursuing optoelectronic device integration on silicon for both in-plane and surface normal optical interconnects using the recess mounting with monolithic metallization (RM³) technique. The waveguides associated with this work provide co-axial optical guiding and coupling for the case of in-plane optical interconnects. These single-mode waveguides have been designed to provide minimum propagation loss and maximum optical coupling to/from an RM³ integrated InGaAsP/InP semiconductor optical amplifier (SOA) or laser. Figure 1 shows a schematic cross-section (in the wafer surface normal and propagation direction plane or y-z plane) showing an integrated SOA and a silicon oxynitride waveguide.

The optimum waveguide design is based on the optimization of a series of tradeoffs such as the tradeoff between maximized coupling and reduced sensitivity to vertical and lateral device misalignment. These design tradeoffs will be illustrated through a series of finite difference time domain (FDTD) simulation results. A typical simulation is shown in Figure 2. Fabry-Perot waveguide loss measurements showing fabricated waveguide propagation losses below 5 dB/cm will also be shown. Finally, the latest experimental results from a recently designed test chip will be included.
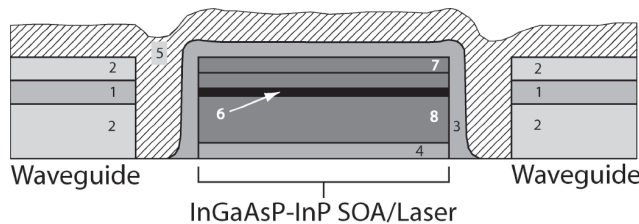
▲ Figure 1: An RM³ integrated SOA/laser schematic: 1) Silicon oxynitride waveguide core, 2) SiO$_2$ waveguide cladding, 3) reflection control material 4) Au/Sn device bonding/contact material, 5) gap-fill material (BCB, Si$_3$N$_4$, or TiO$_2$), 6) InGaAsP core material, 7) SOA/laser ridge, and 8) InP cladding material.
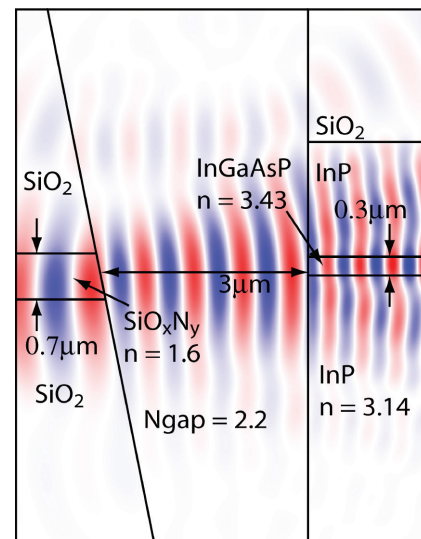
▲ Figure 2: Electric field-strength contour plot taken from a FDTD simulation. This particular simulation shows the optimum silicon oxynitride waveguide parameters for coupling from a waveguide with unintentionally angled sidewalls to an InGaAsP/InP SOA. We are currently exploring TiO$_2$ for use as the high refractive index gap-fill material.

A Bonding Apparatus for OptoPill Assembly

C.A. Cooper, J.M. Perkins, C.G. Fonstad, Jr.
Sponsorship: MARCO IFC, NSF

The central objective of our heterogeneous integration effort is to integrate III-V functionality, such as laser emission, with Si CMOS circuitry in a manner that retains all of the advantages of multi-wafer, batch processing that have propelled Si ICs along the Moore's Law performance timeline for so long. To this end we have developed recess mounting with monolithic integration (RM^3), in which we place III-V heterostructure pills, OptoPills, in recesses 5 to 6 microns deep and 50 microns in diameter that are formed in the inter-metal dielectric layers covering a processed Si IC. We then interconnect them monolithically with the underlying circuitry.

Once the heterostructure device pills have been placed in their recesses, whether by means of micro-scale pick and place or fluidic self-assembly (both described in other abstracts), they must be securely fastened in place. It is also often desired that a good electrical contact be made to the bottom of the pill at the same time. Two different solders have been found to be particularly suitable for this purpose: a Au-Sn eutectic to solder gold-coated pills into the recesses, and a Pd-Sn-Pd stack to bond bare pills into the recesses. In both cases it is necessary to supply pressure between the pill and substrate to reliably achieve successful bonding or soldering. To apply the required pressure to these micro-scale pills, particularly when they are in recesses, we have developed a bonding system, shown in Figure 1, in which a vacuum-bagging film and a pressure differential are used to apply a controlled, reproducible, and uniform pressure simultaneously to all the pills on a wafer. A photograph of the unit, with the outer chamber removed so the film is visible, is shown in Figure 2. Typical bonding conditions used involve a pressure of approximately 50 psi and a temperature of approximately 200°C.
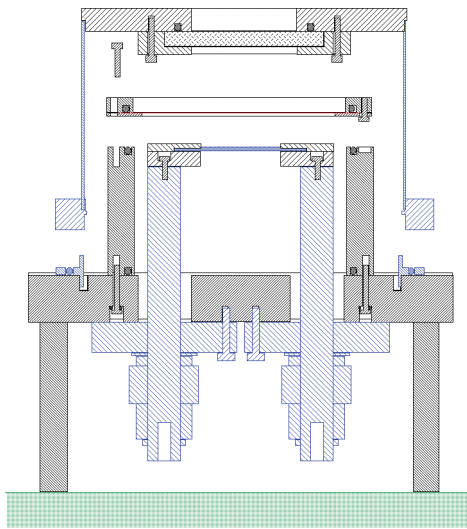
▲ Figure 1: Cross-sectional drawing of the bonding chamber showing the base plate with heater strip, the inner bonding-ambient chamber, the film holder plate, and the outer pressurized chamber.
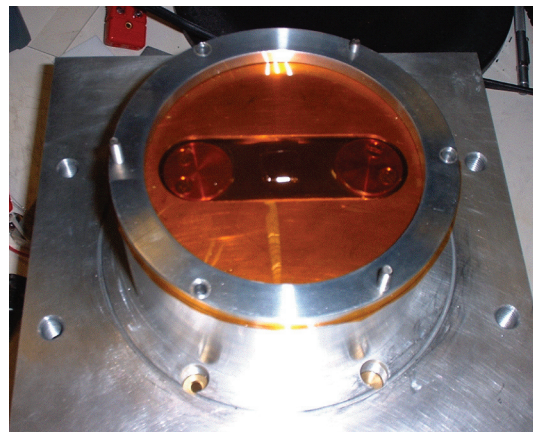
▲ Figure 2: The film-pressure bonding system shown with the outer, pressurized chamber removed to show the film and heater strip.

REFERENCES

[1] M.S. Teo, "Development of pick-and-place techniques for monolithic OptoPill integration," Master's thesis, Massachusetts Institute of Technology, Cambridge, 2005.

Micro-scale Pick-and-Place Integration of III-V Devices on Silicon

J.M. Perkins, C.A. Cooper, C.G. Fonstad, Jr.
Sponsorship: MARCO IFC, NSF

We are developing micro-scale assembly techniques for integrating III-V optoelectronic devices on silicon integrated circuits that blur the practical distinction between hybrid and monolithic integration. Our general approach, which we term Recess mounting with monolithic integration (RM^3) involves forming recesses 5 to 6 microns deep and 50 microns in diameter, in the inter-metal dielectric layers covering a processed Si IC. After all of the standard silicon processing is completed, the Si IC wafers for RM^3 integration undergo further back-end processing first to create the recesses, and to then place and bond III-V device structures in them. Wafer-level processing is then continued to complete any remaining III-V device processing and to interconnect those devices with the underlying electronic circuitry. One approach we have taken to placing the III-V devices in recesses has been to form discrete heterostructure pills the size of the recesses, and the then place them individually into the recesses using micro-scale pick-and-place assembly, as illustrated in Figure 1.

The dimensions of the pills we are assembling are much smaller than the die normally encountered in pick-and-place applications, and thus conventionally available vacuum pick-up tools are not suitable. We have found, however, that quartz micropipettes of the type used by microbiologists to study cells can be fabricated with the right dimensions and geometry for this application. In particular, we use micropipettes pulled from 1-mm-diameter, 0.25-mm-wall quartz tubing and tapered down over 7 mm to a tip diameter of 30 microns. The tip is beveled at 45° to complete the pick-up tool. A photomicrograph of a tool mounted in its holder is shown in Figure 2. With this tool, pills can be picked up, placed in a recess, and released without damaging the pills [1]. Our current effort is directed at both using micro-scale pick and place to do heterogeneous integration, and further developing and refining the technique.

▲ Figure 1: A cartoon illustrating the micro-scale pick and place process for locating a heterostructure device pill in a recess on a Si IC wafer surface.

▲ Figure 2: A quartz micropipette pick-up tool mounted on its holder.
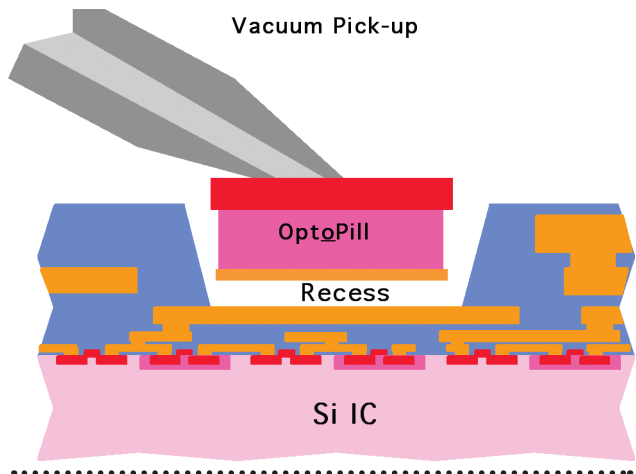
PHOTONICS

229

REFERENCES

[1] M.S. Teo, "Development of pick-and-place techniques for monolithic OptoPill integration," Master's thesis, Massachusetts Institute of Technology, Cambridge,2005.

# AlGaAs/GaAs VCSEL Processing and Heterogeneous Integration with Si ICs

J.M. Perkins, C.G. Fonstad, Jr.
Sponsorship: MARCO IFC

The goal of this research is to integrate AlGaAs vertical cavity surface-emitting lasers (VCSELs) onto a preprocessed Si IC, enabling creation of an intimately integrated hybrid circuit of CMOS devices and III-V laser diodes for interconnect applications. Pick-and-Place integration as well as magnetically assisted statistical assembly will be used [1-2]. These techniques will insert the III-V devices onto the target IC. These devices can then be solder-bonded in place, securing and electrically connecting them to the IC.

A technique, using AlGaAs 850 nm VCSEL heterostructure device material to produce optopills, has been developed to allow this hybrid integration. Mesa etching, ohmic metalization, current aperture formation, and selective removal have been studied. Oxide aperture growth has been performed and a non-invasive technique has been developed to characterize these oxide current apertures. Low-resistance contacts have been obtained, producing devices with 1.5-volt turn-on voltages. I-V, L-I, and spectral characteristics have been obtained and lasing is observed. A technique has been developed to metalize and pattern the backside of these devices, enabling metal-metal integration bonding, as well as enabling the inclusion of a backside magnetically susceptible Ni layer needed for MASA integration. Fully processed pill devices have been obtained. A CMOS neural network IC has been designed and fabricated [3].

Initial integration work has begun. Recesses have been made opening to an aluminum backplane and a Au/Sn stack has been patterned within the recesses to provide a bonding alloy. The VCSEL pills have been metalized with a stack that includes a Au top-bonding layer, using the backside liftoff technique. They have been placed within these recesses metal-side down. These devices can be maneuvered to center them within the wells. A modified bonding scheme has been developed and successfully used to bond these devices and anneal their contacts. A polymer film presses down on the pills at 30 psi to produce the compressive force needed in the Au/Sn bonding process. An Al film between the sample and the polymer pressure film has been used to prevent the devices from sticking to the polymer and ripping them off after bonding. The bonded devices have been shown to be connected to the aluminum backplane and to have good device characteristics. A novel post bonding passivation and metalization scheme has been developed and will be tested. Heat dissipation modeling is being developed to determine the operation temperature of these devices and how it depends on the surrounding circuitry environment.
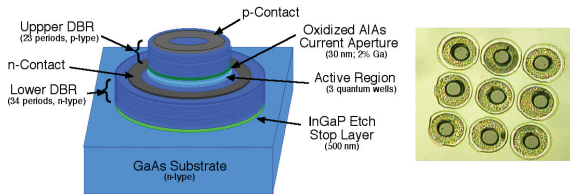
▲ Figure 1: (left) Diagram of a VCSEL opto-pill processed until the release step. First mirror etch exposes n-type layer for metalization, while also exposing the aperture layer for wet oxidation. Top metalized contacts allow prerelease device characterization. (right) Bonded pills in Al recesses. No aperture or top metallization.
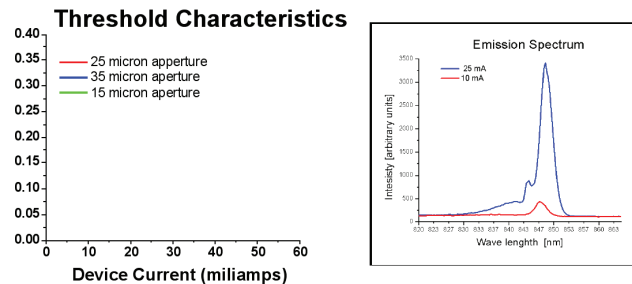
▲ Figure 2: (left) Luminescence characteristics of apertured VCSEL devices on native substrate. (right) Emission spectrum for 10 and 25 milliamps device currents for a nonapertured 35 micron device.

REFERENCES

[1] C.G. Fonstad, "Magnetically assisted statistical assembly - a new heterogeneous integration technique," Singapore-MIT Alliance Symposium, Jan. 2002.

[2] M. Teo, "Development of pick and place assembly techniques for monolithic optopill integration," Doctoral thesis, Massachusetts Institute of Technology, Cambridge, 2005.

[3] T. Simpkins, "Design, modeling, and simulation of a compact optoelectronic neural coprocessor," Master's thesis, Massachusetts Institute of Technology, Cambridge,2005

# Highly Integrable In-Plane Laser Diodes for Optoelectronic Integration

J.J. Rumpler, E.R. Barkley, J.M. Perkins, C.G. Fonstad, Jr.
Sponsorship: DARPA

The level of integration seen in commercial active photonic devices is at most a laser monolithically integrated with a modulator or a photodetector flip-chip bonded to an optical waveguide. Our goal is to achieve much larger levels of optoelectronic integration, and our approach involves optimally fabricating building blocks, such as laser diodes or optical amplifiers, and assembling these blocks in dielectric recesses on a system substrate [1]. Our test case for demonstrating this technology is the integration of 1.55 µm InGaAsP edge-emitting laser diode blocks with planar silicon oxy-nitride waveguides on silicon.

To this end, a process has been developed to fabricate freestanding edge-emitting laser diodes by our newly developed micro-cleaving technique. This process begins with a (100)-oriented InP wafer upon which an in-plane laser heterostructure has been grown. After defining the laser ridge on the top-side of the substrate, the wafer frontside is patterned into large arrays of rectangular bars aligned with the laser ridges and wafer flat so that short and long faces of the rectangular bars are aligned with the two cleavage planes as shown in Figure 1. Notches in the rectangular bars divide each rectangular bar into three rectangular sub-bars in between two square sub-bars. The rectangular sub-bars define the active devices, L1, L2, and L3, and the square sub-bars at the ends define dummy devices D1 and D2.

Once the bar pattern is formed on the semiconductor wafer, a chemical-etch resistant layer is applied to the wafer surface and the semiconductor substrate is removed using a hydrochloric acid-based, selective wet-etch chemistry that stops on an InGaAs etch stop layer. The etch-resistant layer is then dissolved and the long bars are collected in solution. The long bars are then agitated ultrasonically in this solution at which time they preferentially cleave in the notch region forming a large quantity of active devices and dummy devices. An individual cleaved laser platelet is seen in Figure 2.
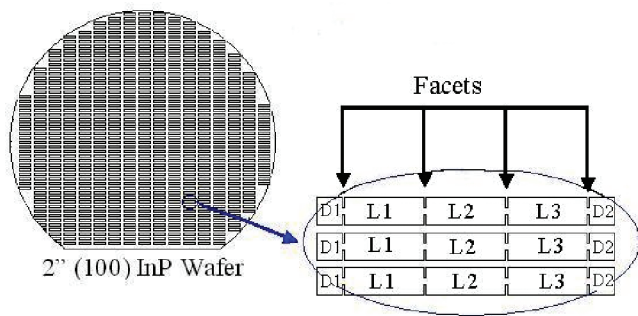
▲ Figure 1: Schematic depicting the micro-cleave enabling pattern and how it must be aligned properly to the semiconductor.
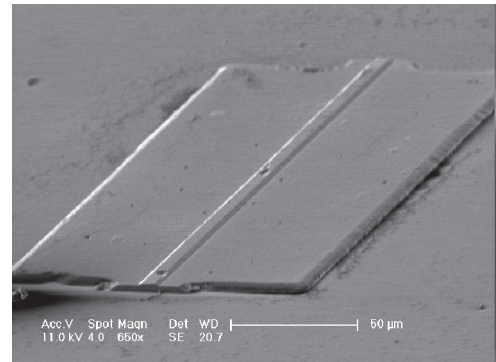
▲ Figure 2: SEM image of a micro-cleaved edge emitting laser platelet with a ridge defined.

REFERENCES

[1]   J.J. Rumpler, J.M. Perkins, and C.G. Fonstad, Jr., "Optoelectronic integration using statistical assembly and magnetic retention of heterostructure pills," in *Proc. of the Conf. on Lasers and Electro-Optics (CLEO)*, vol. 2, 16-21, pp. 2, May 2004.

Magnetically Assisted Statistical Assembly of III-V Devices on CMOS

J.J. Rumpler, J.M. Perkins, C.G. Fonstad, Jr.
Sponsorship: MARCO IFC, NSF

Development of an efficient process for integrating III-V devices on silicon CMOS is key to making optical interconnects a reality on the micro-scale as well as enabling low cost and compact optoelectronic sensors for applications such as biomedicine. The III-V semiconductors typically have superior lasing properties and high electron mobilities making make them attractive for applications such as optical sources and RF electronics. Silicon is the material of choice for large-scale digital circuits because of its ability to form a high-quality, low-defect oxide, thus enabling low-power CMOS technology. Unfortunately, direct epitaxy of III-V devices on silicon is not practical due to mismatches between the lattice constant and thermal expansion coefficient of the materials. Therefore, III-V device integration on CMOS today consists of at most small arrays of devices attached by flip-chip or wire bonding. Our approach is aimed at permitting large-scale integration of these heterogeneous materials. Specifically, III-V and silicon devices are processed separately under optimal conditions on their own native substrates. On the CMOS wafer surface, dielectric recesses are formed. At the bottom of these recesses are located patterned permanent ferromagnetic films. Once fabricated, the III-V devices having a permeable ferromagnetic film are released from their substrate and flowed over the CMOS wafer where they assemble in the recesses by gravity and are retained by short-range magnetic forces. Experimentally, the III-V devices are found to stick to the permanent magnetic film due to the large magnetic adhesion force [1].

Experiments have been conducted whereby thousands of these 45-micron diameter, 6-micron thick III-V devices are flowed over a target substrate consisting of hundreds of correspondingly sized dielectric recesses as shown in Figure 1. Initial fluidic assembly experiments without magnetic retention show that a large number of successfully assembled pills, as shown in Figure 2. They are also found to readily come out of the recesses as the substrate is removed from the fluid, which verifies the need for a short-range retention force.
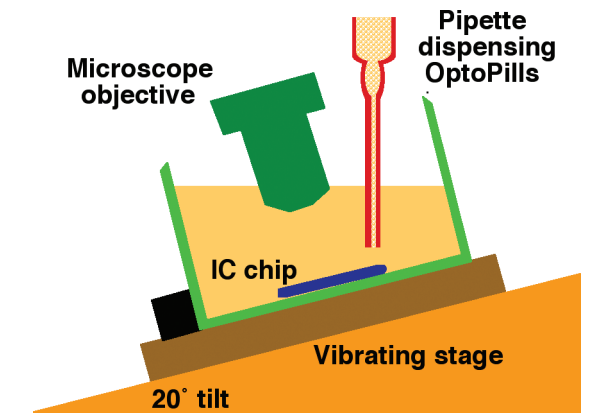
▲ Figure 1: Assembly setup.
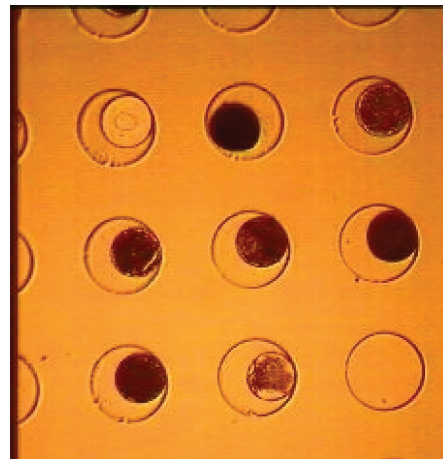
▲ Figure 2: An array of silicon dioxide recesses filled by GaAs devices.

REFERENCES

[1]   J.J. Rumpler, J.M. Perkins, and C.G. Fonstad, Jr., "Use of patterned magnetic films to retain devices during fluidic self-assembly," manuscript in preparation.

Development of Terahertz Quantum Cascade Lasers

B. Williams, H. Callebaut, S. Kumar, Q. Qin, Q. Hu (in coll. with J. Reno, Sandia National Laboratories)

The terahertz frequency range (1-10 THz) has long remained undeveloped, mainly due to the lack of compact, coherent radiation sources. Transitions between subbands in semiconductor quantum wells were suggested as a method to generate long wavelength radiation at customizable frequencies. However, because of difficulties in achieving population inversion between narrowly separated subbands and mode confinement at long wavelengths, THz lasers based on intersubband transitions were developed only very recently. We have developed THz quantum-cascade lasers based on resonant-phonon-assisted depopulation and using metal-metal waveguides for mode confinement. Figure 1 illustrates the schematics of both features are illustrated. Using the combination of these two unique features, we have developed many THz QCLs with record performance, including a maximum pulsed operating temperature at 164 K (see Figure 2), a maximum power of ~250 mW, and the longest wavelength (~161 μm) QCL to date without the assistance of magnetic fields.
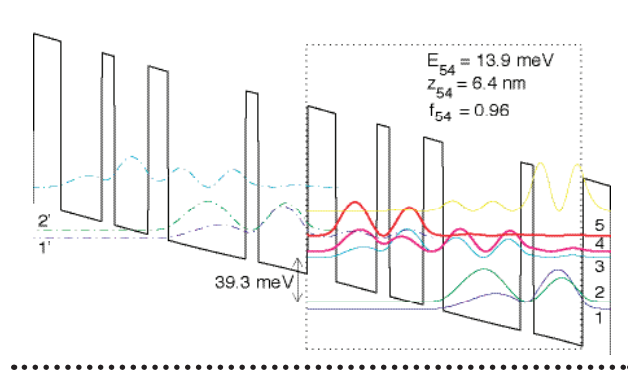
▲ Figure 1
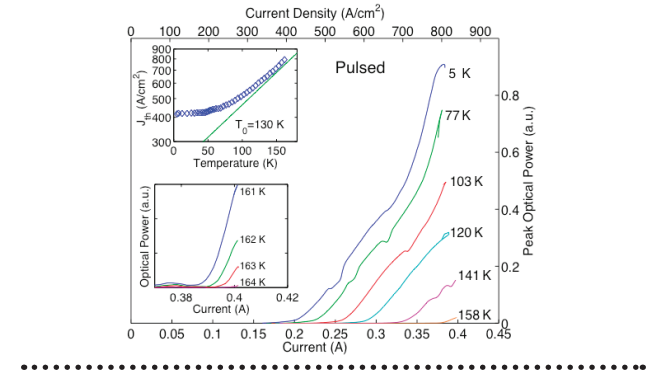
▲ Figure 2
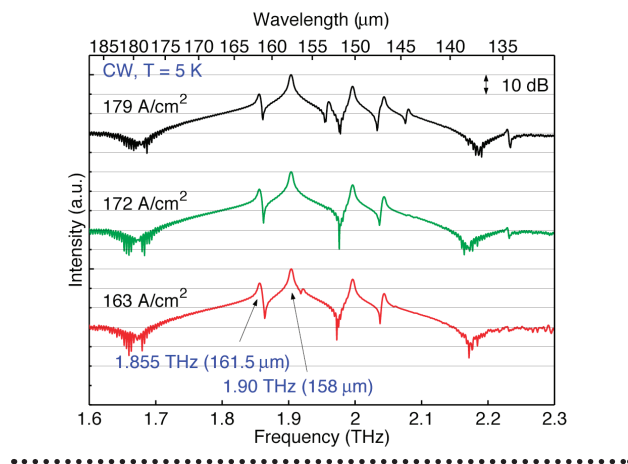
▲ Figure 3
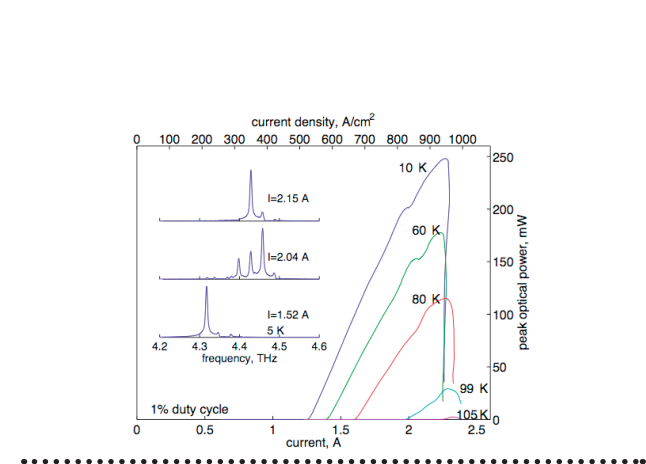
▲ Figure 4

Broadband, Saturable Bragg Reflectors for Mode-locking, Ultrafast Lasers

G. Petrich, F. Kaertner, E. Ippen, L.A. Kolodziejski

Self-starting, mode-locked, ultrafast lasers require broadband high reflectivity mirrors with saturable absorbers. However, AlAs/GaAs or AlAs/AlGaAs mirrors with saturable absorbers exhibit a limited bandwidth due to the low index-contrast between the individual GaAs and AlGaAs layers, but these mirrors are suitable for mode-locking 1064-nm lasers. Figure 1 shows the reflectivity, as measured using a Varian Cary 500i spectrophotometer, and the room temperature photoluminescence from a saturable Bragg reflector (SBR) consisting of 25 pairs of 88-nm-thick $Al_{0.95}Ga_{0.05}As$ layers and 74.7-nm-thick GaAs layers with two 8-nm-thick $In_{0.27}Ga_{0.73}As$ quantum wells separated by 16 nm of GaAs centered within 117 nm of GaAs. The dip in the reflectivity that is due to the InGaAs quantum wells is easily observed.

In addition, two oxidizable saturable Bragg reflectors have been grown by molecular beam epitaxy. The SBRs consist of two 8-nm-thick InGaAs quantum wells separated by GaAs with GaAs cladding layers on a 7-pair oxidizable InGaP/AlAs dielectric stack. By thermally oxidizing the AlAs layers to form Al_xO_y, broadband reflectors can be created. The photoluminescence that is measured from the as-grown SBRs exhibit emission at 1062 +/- 2 nm. The AlAs/InGaP mirror stacks have not been oxidized thus far.
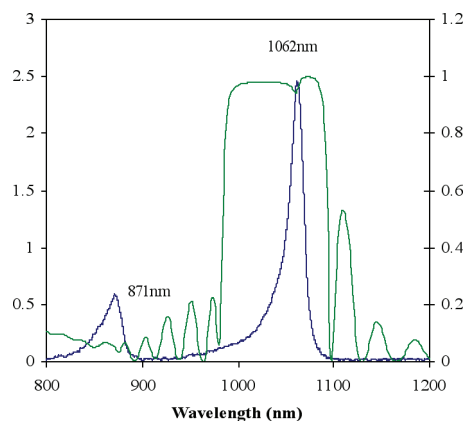
▲ Figure 1: The reflectivity and photoluminescence of an InGaAs/GaAs absorber on an AlGaAs/GaAs distributed Bragg reflector.

A Nanoelectromechanically Tunable, High-Index-Contrast Interference Directional Coupler

R.E. Bryant, M.L. Povinelli, S.G. Johnson, G.S. Petrich, J.D. Joannopoulos, E.P. Ippen, L.A. Kolodziejski

One of the most exciting and practical application of a directional coupler is the switch modulator in which the amount of optical power coupling is adjustable. A method of tuning a single mode interference high-index-contrast (HIC) directional coupler with a nanoelectromechanical (NEM) mechanism is proposed. An electomechanically tunable directional coupler has the benefit of providing large changes in effective index, of being transparent, and requiring low power. An HIC system has the added benefit of permitting a size reduction that allows machined nanostructures to optically guide light at a wavelength of 1.55 microns as well as to mechanically actuate.

Using GaAs waveguides with a ~300-nm-square cross-section, directional couplers are fabricated so that they are anchored atop of Al_xO_y as well as suspended over a trench. The anchored portions of the waveguides are adiabatically curved to a lithographically-defined coupling separation that exists suspended over the trench. The desired mechanical compliance determines the extent to which the adiabic curves are situated over the trench. The amount of optical power coupling is adjusted by the electromechanical actuation of the waveguide separation and the S-bend curvature. The selected method of electromechanical actuation utilizes a gap-closer mechanism. A gap-closer is a "spring"-suspended, parallel capacitive plate mechanism that is allowed to mechanically deflect in order to reduce its capacitance. In planar MEMS/NEMS, the "spring" is usually a mechanical compliant beam (i.e., the suspended portion of the directional coupler). Gap-closers are characterized by large mechanical force densities over small displacements, which make them well suited for this particular application.

Molecular beam epitaxy is used to define layer thickness. Traditional micromachining techniques are used to lithographically define the topology and provide optical, electrical, and mechanical isolation. After these processes, high-index-contrast is accomplished by stream oxidation that transforms crystalline high Al-content $Al_xGa_{1-x}As$ alloys to an amorphous Al_xO_y oxide. Nanostructure mechanical latches and bi-stable mechanisms are expected to aid in improving alignment accuracy. Nanostructure mechanical levers can be used to tailor the shape and angle of deflection. The device is expected to operate within the MHz regime in a speed-optimized design.

Electrically-Activated Nanocavity Laser Using One-Dimensional Photonic Crystals

A. Grine, G.S. Petrich, L.A. Kolodziejski
Sponsorship: NSF-MRSEC

The focus of this project is the design and fabrication of a laser that is suitable as a light source for integrated optics. Four characteristics make the laser particularly advantageous for use in integrated optics. First, the laser is electrically activated and eliminates the need for a separate pump laser. Second, the laser requires only 25 μm^2 of space, which conserves chip real-estate and should lead to a relatively small threshold power. Third, the output of the laser is directly connected to the output waveguide, eliminating the need for separate couplers. Finally, the laser's output is coplanar, which eases integration with other components.

The laser design (Figure 1) incorporates one-dimensional (1-D) photonic crystals patterned on two crossing waveguides. The nanocavity, located at the two waveguide's intersection, creates a high-Q optical resonator with the 1-D photonic crystals acting as highly reflective mirrors. By removing some of the holes in one of the photonic crystals, one can control the direction of the emitted light. The top GaAs-based waveguide is doped p-type, while the bottom, InGaAlP-based waveguide, is doped n-type, so that a p-n diode exists only in the area where the waveguides overlap. The top GaAs waveguide contains a quantum dots-in-a-well structure, which serves as the active material for the laser. Optical simulations have led to the inclusion of a high-index InGaP layer in the center of the output waveguide. The inclusion of the InGaP layer allows more light to be coupled into the output waveguide and a thinner upper waveguide to be used to minimize the loss due to radiation. The output waveguide is designed to be multi-mode in order to minimize the fabrication time.

A new fabrication sequence has been developed that employs either electron-beam or focused-ion-beam lithography to define the sub-micron features and photolithography to define the larger features, allowing many lasers with varying dimensions to efficiently be processed on a single chip. A die measuring ~ ¼" x ¼" contains 280 devices, each with varying features. This method will allow the empirical determination of the optimal device. To ease the electron-beam lithography process, the mask unit cell contains an array of six devices to be processed within a 200-μm square electron-beam field (Figure 2). Current work includes the fabrication of the device in the Technology Research Laboratory. Once the device is fabricated, testing will take place in collaboration with the Ultrafast Optics and Quantum Electronics Group.
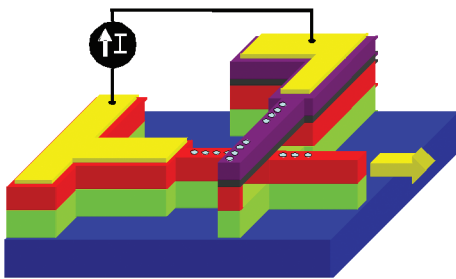
▲ Figure 1: Depiction of the electrically-activated, photonic-crystal nanocavity laser. The green arrow represents the direction and location of the emitted light.
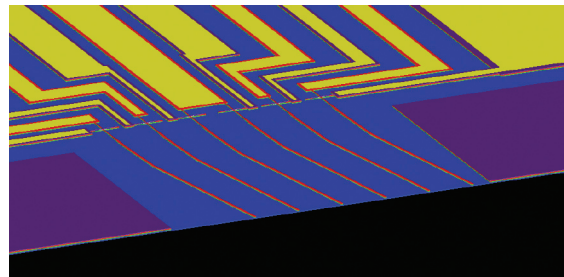
▲ Figure 2: Schematic of an array of 6 lasers within a 200-μm field. The output waveguide is 164 μm long and is angled 11˚ with respect to the facet.

# Photonic Integrated Circuits for Ultrafast Optical Logic

R. Williams, A. Markina, G.S. Petrich, E.P. Ippen, R.J. Ram, L.A. Kolodziejski
Sponsorship: DARPA

With an increasing demand for higher speed switching technologies in optical telecommunications networks, interest in both all-optical switching schemes and monolithic integration of photonic components is increasing. Reducing or eliminating optical-electronic-optical (OEO) conversions offers advantages of higher bit rates, lower power consumption, and reductions in size and weight.

The current study aims to demonstrate an optical gate consisting of semiconductor optical amplifiers (SOAs) integrated into a Mach-Zehnder interferometer on InP substrates. The optical gate is capable of basic Boolean functionality, wavelength conversion, and other important switching operations. Prior to fabrication, the design of the components such as the InGaAsP quaternary dilute waveguide, the multi-mode interferometers, and the adiabatic taper geometry has been optimized using standard optical simulation techniques.

To integrate the active SOA devices with the passive components, an asymmetric twin waveguide approach, which eliminates the need for regrowth at the expense of additional processing steps, is employed. The first-generation design contained two separate die: one consisting of basic isolated components and the other consisting of integrated components (Figure 1). Upon the completion of the processing and testing, further optimizations of the design and fabrication process were incorporated into a second-generation design that is currently undergoing fabrication on campus and in collaboration with Lincoln Laboratory. The second-generation design combines both the active and passive devices into single die suitable for a step-and-repeat mask set, allowing for sharper tapers and smoother waveguide bends. Processing improvements include depositing the base metal for the top-side contact prior to any III-V etching, minimizing the amount of InP-based etching through the use of trenches, and using a dedicated CH_4/H_2 etcher at Lincoln Laboratory. Figure 2 shows the tips of the upper active waveguide and the trench in which the passive waveguides will be centered.
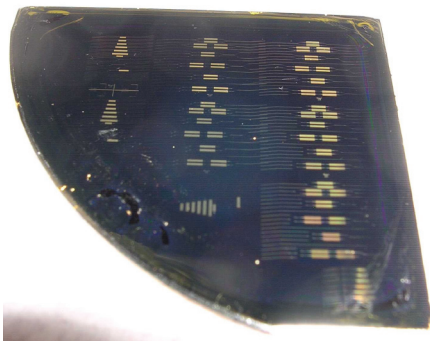
▲ Figure 1: A photograph of the first-generation fabricated dies on a quarter of a 2" InP wafer.
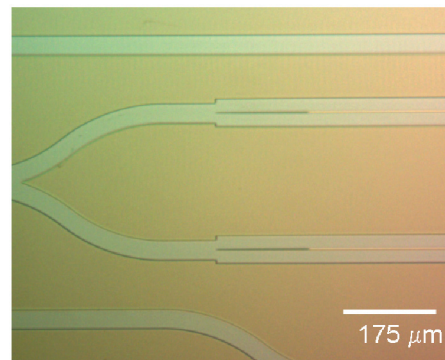
▲ Figure 2: A photograph of the beginning of the second-generation Mach Zehnder interferometer.

PHOTONICS

Super-collimation of Light in Photonic Crystal Slabs

S.N. Tandon, M. Dahlem, P. Rakich, M. Ibanescu, M. Soljacic, G.S. Petrich, J.D. Joannopoulos, E.P. Ippen, L.A. Kolodziejski
Sponsorship: NSF-MRSEC, MARCO IFC

A super-collimator is a device in which light is guided by the dispersion properties of a photonic crystal slab rather than by defects or by traditional waveguiding structures. Photonic crystals (PhC) form the essence of the super-collimation effect. The super-collimator consists of a two-dimensional PhC composed of a square lattice of cylindrical air holes etched into a high-index material such as silicon. The device was fabricated using a silicon-on-insulator wafer in which the low-index oxide layer (3 μm thick) is used to minimize radiation loss into the high-index silicon substrate. The photonic crystal occupies the entire surface of the super-collimator so that the cleaved edges of the photonic crystal function as input or output facets of the device. The initial design has focused on realizing super-collimation at a wavelength of 1500 nm so that the hole lattice constant, hole radius, and Si thickness were 350 nm, 105 nm and 200 nm, respectively.

Testing of the super-collimator device has been performed in collaboration with the Ultra-fast Optics Group. Figure 1 shows the output of the propagating beam from a cleaved facet after traversing the PhC for 5 mm where the 1-μm-diameter incident optical beam exiting the device was found to be 2-μm wide. By defining the isotropic diffraction length to be the length over which the light beam spreads by root 2, super-collimation for more than 600 isotropic diffraction lengths has been observed. Using an infrared-camera to image the scattered light, the light propagating through the photonic crystal was observed at a number of different wavelengths. Figure 2a-c shows the simulated propagation of light through an ideal photonic crystal, while Figure 2d-f shows the measured scattered light as the light propagated through the super-collimator. Figure 2e shows that at a normalized frequency of $\omega=0.233$ ($\lambda=1510$ nm), light propagates through the photonic crystal in a collimated fashion as the light path resembles a stripe of light. As the normalized frequency of the input laser is varied from $\omega=0.233$, the beam no longer exhibits a collimated behavior and begins to diverge, with the beam width expanding as it propagates. The inclusion of short-range, fabrication-related disorder can improve the agreement between the measured light propagation and the simulated results (Figure 2g-i).
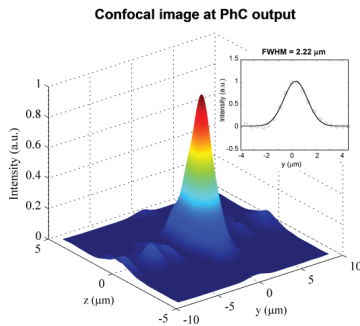
▲ Figure 1: Output measured at the facet of the device for a super-collimating beam that has propagated for 5 mm inside a photonic crystal silicon slab.
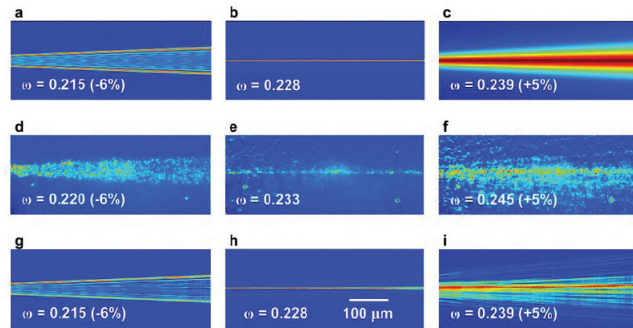
▲ Figure 2: (a-c) Theoretical beam evolution generated by the beam propagation method to be compared with experiment d-f. (d-f) Top-view experimental images of light traveling through the photonic crystal at wavelengths of 1430 nm, 1510 nm and 1610 nm that were obtained from an IR camera. g-i, Simulations of the beam evolution including the effects of short-range disorder.

Tunnel Junction Diodes

S.Y. Young, R.D. Williams G.S. Petrich, R.J. Ram, L.A. Kolodziejski
Sponsorship: DARPA

The goal of this project is to characterize the tunneling behavior in InGaAs/GaAs tunnel junction diodes for use in tunnel-junction-coupled lasers. The reversed-bias leakage current of the tunnel junctions can be exploited to epitaxially connect more than one lasing active region in series. The tunneling of electrons from the valence band of one active region to the conduction band of a second active region can increase the external quantum efficiency of the overall device by allowing multiple photons to be emitted per injected carrier. Thus, low tunneling resistances are desired for high-efficiency lasers.

The InGaAs/GaAs tunnel junction diodes were grown with varying indium contents ranging from 6.5% to 13.5% while the diameter of the fabricated diode mesas ranged from 3.5 μm to 90 μm. Variable-angle spectroscopic ellipsometry was performed on the epiwafers to determine the InGaAs composition and the epilayer thickness. Under both forward and reverse bias, the InGaAs tunnel junction diodes matched the theoretically predicted electrical behavior. First, the tunneling resistance decreased for increasing contact size, but, more importantly, the resistance decreased with increasing indium content (Figure 1).

The results demonstrate that more electrons tunnel across the tunnel junction as the amount of indium is increased due to the decrease of the InGaAs bandgap. Additional tests also demonstrated that annealing the metal-semiconductor contact reduced the diode's overall resistance and that reducing the diode's temperature increased the tunnel junction resistance. With tunneling successfully demonstrated, the InGaAs tunnel junctions were implemented in GaAs-based, two-stage lasers. Significant increases in efficiency of the tunnel-junction-coupled lasers are anticipated in future work.
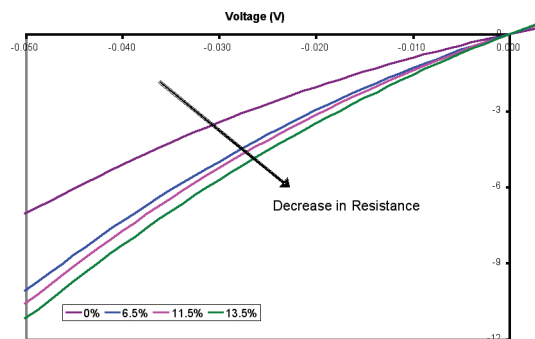
▲ Figure 1: The reverse-bias current-density response, demonstrating a decrease in resistance for increasing indium content.

Ultrabroadband Modulator Arrays

G.S. Petrich, F.X. Kaertner, E.P. Ippen, L.A. Kolodziejski
Sponsorship: DARPA

Creating an arbitrary optical waveform at wavelengths that are centered at 800 nm requires an ultrabroadband modulator array. Since these modulators operate at wavelengths around 800 nm, the material choices are limited to relatively high-Al content AlGaAs and $In_{0.5}(Ga_xAl_{1-x})_{0.5}P$ layers lattice-matched to GaAs. In addition, since GaAs absorbs light with a wavelength less than 870 nm, the lower cladding layer of the modulator must be relatively thick to isolate the modulator from the GaAs substrate. To create the largest optical mode possible and to minimize the coupling loss, the index contrast between the waveguiding layers and the cladding layers should be minimized. Hence, a dilute waveguide structure in which thin layers of high index material are embedded in a low-index material, is employed. The resulting layered structure has an effective index slightly higher than the low-index material and is determined by the layer thicknesses as well as the refractive index of the two materials that compose the dilute waveguide. Two slightly different structures were grown by molecular beam epitaxy: (i) an InAlP-based structure in which the dilute waveguide consisted of alternating layers of InAlP and $Al_{0.5}Ga_{0.5}As$ and (ii) an $Al_{0.8}Ga_{0.2}As$-based structure in which the dilute waveguide consisted of alternating layers of $Al_{0.8}Ga_{0.2}As$ and InGaP. Both structures are challenging in terms of the epitaxial growth. In the phosphide-based structure, the growth of thick, lattice-matched InAlP cladding layers is challenging due to the need to maintain the lattice-matched condition and due to possible anion ordering. In the arsenide-based structure, although the use of $Al_{0.8}Ga_{0.2}As$ for the cladding layer minimizes the lattice-mismatch problem, achieving high-quality, high-Al content AlGaAs cladding layers is difficult due to the low Al adatom mobility on the surface during growth. To minimize free carrier loss, the modulator uses a p-i-n structure in which the Si and Be dopants are graded from the contact layers to the dilute waveguide region. Photoluminescence (PL) measurements from the arsenide-based structure show a weak PL peak at ~650 nm from the InGaP layers in the dilute waveguide. The $Al_{0.8}Ga_{0.2}As$ and $Al_{0.5}Ga_{0.5}As$ layers as well as the InAlP layers have indirect band gaps and hence do not exhibit photoluminescence. Due to the high etch selectivity between the arsenide and phosphide layers, the uppermost high index layer of the dilute waveguide also acts as an etch stop.

Both structures are anticipated to have similar optical mode profiles; the structures are designed to be single mode in a 2-μm wide ridge waveguide. Using OptiBPM, the fundamental mode for the phosphide-based structure is calculated to be roughly 2 μm x 1 μm (WxH); a similar mode profile exists for the arsenide-based structure. In both structures, if the dilute waveguide is not completely etched, due to the low index contrast of the dilute waveguides, the bending radius is quite large, on the order of a millimeter.

A mask set suitable for both structures has been designed and fabricated. The mask set contains Mach Zehnder interferometer modulators of various lengths with multimode interference couplers or Y-splitters. The Mach Zehnder interferometer modulators as well as conventional modulators are oriented both parallel and perpendicular to the major flat of the 2" GaAs(100) wafers. The mask set also contains a variety of passive components such as Y-splitters and multimode interference couplers as well as straight and curved waveguides. The fabrication of the phosphide-based and arsenide-based modulators will commence shortly.

Design and Measurement of Thermo-optics on Silicon

R. Amatya, R.J. Ram

The vision of optoelectronics started with the integration of optics and electronics on the same substrate. Various optical and electrical components on the same chip would have better performance and functionalities than the components taken alone. Electrical integrated circuits (IC) have been very successful on silicon substrate. Thus, silicon is one of the more desirable materials for optoelectronic devices. Silicon (Si) as well as silicon nitride (SiN) optical waveguides are becoming integral components for optical systems because of their advantages of high index contrast and compatibility with IC. Thermally tunable optical ring resonators made of SiN on silicon can be used as switches and filters. A small ring diameter ($\approx$20 μm) allows a large free-spectral range. The temperature dependence of the refractive index (i.e., the thermo-optic effect of the core and cladding) is utilized to tune these ring resonators. Resistive heaters are designed to sit on top of the cladding for thermal tuning. One of the key aspects while designing the heaters is minimum power dissipation per GHz in terms of tuning flexibility. Figure 1 shows a thermal simulation for a heater over a two-ring filter.

Waveguides formed on silicon-on-insulator substrates can have sub-microsecond switching capabilities. These waveguides are heated by passing current through them; it is important to be able to study and measure the thermal characteristics of the device. Thermoreflectance spectroscopy is one of the many ways of measuring the temperature of the device. A temperature profile for a silicon-melt waveguide of 0.5 μm thickness is shown by measuring the reflectance changes due to modulating the current. Figure 2 shows the image of the melt waveguide along with temperature profile and the thermoreflectance image. The figure on the left inset shows the non-uniform temperature distribution within the waveguide. For the silicon melt waveguide, the measured thermo-optic coefficient (κ) was 1.1E-4/K, which is similar to the reported values for silicon for the specific wavelength (510 nm). Similar measurements can be done on SiN ring resonators to obtain the thermo-optic coefficient.
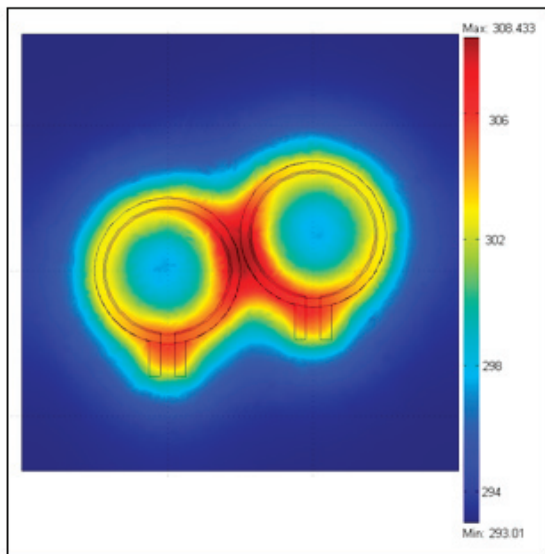
▲ Figure 1: Temperature profile for the thermal tuning of ring resonators.
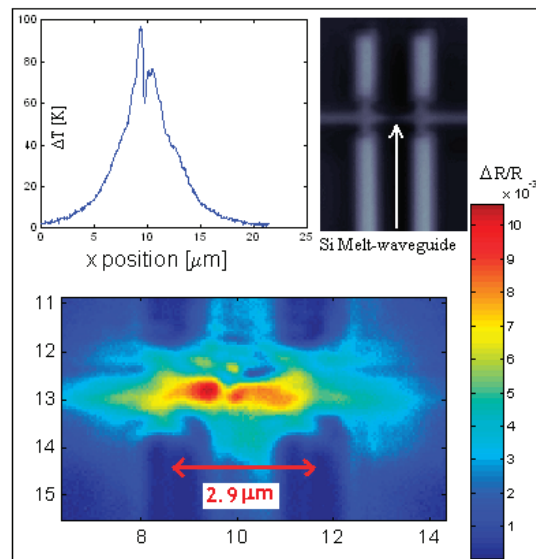
▲ Figure 2: Silicon melt waveguide-thermal profile using the thermo-reflectance technique.

Polymer Waveguides for Integrated Biosensors

K. Lee, R.J. Ram

To overcome the challenge of fabricating large-dimension waveguides with optical-quality surfaces, a conventional fabrication approach using plastics is utilized over a micro-fabrication approach generally used for micro-fluidics. While conventional milling can easily create structures with dimensions of 1 mm, roughness from the fabrication process leads to diffuse surfaces and variations greater than 1 μm. To overcome the roughness due to milling and ultimately create large features with optical quality roughness, a solvent vapor polishing process is used in which a solvent vapor such as methylene chloride vapor is used to liquify

Fabricated waveguides exhibit a propagation loss of 0.136 dB/cm at 626 nm and a measured 50% intensity numerical aperture of 0.5. E-beam deposited silver on PDMS measured a reflectivity of 72% with a HeNe laser at 632 nm. Oxygen measurements were preformed by fiber coupling amplitude modulated LEDs into the input guides, collecting the output through a colored glass filter and photodetectors, and measuring the phase shift between the input and output signals. The sensor system achieves an SNR greater than 40 and provides a phase shift of 30 degrees with 1 degree variance from nitrogen to air.
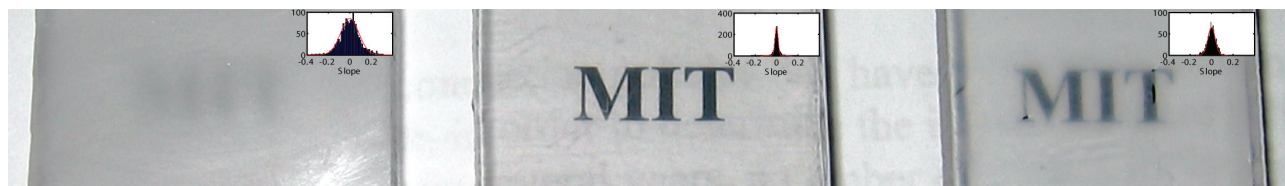
▲ Figure 1: Polished polycarbonate samples under different polishing conditions and histograms of the slope distribution seen at the surface. (Left) 10% saturation pressure results in no polishing (Ra = 1000 nm). (Middle) 75% saturation pressure results in excellent polishing (Ra = 70 nm). (Right) 95% saturation pressure results in over-polishing (120 nm) and is seen as a developing haze.

the plastic surface [1]. Varying the solvent pressure and the exposure time can control the degree of polishing. Under optimal polishing conditions, the average roughness from sanded polycarbonate samples can be reduced from 1000 nm to 70 nm as shown in Figure 1. When combined with vapor polishing, CNC milling becomes a viable process for both optical and micro-fluidic fabrication of master molds.

After mold fabrication, standard soft lithography processes are used to create negative PDMS replicas of the polycarbonate molds. In addition, PDMS molds are subject to e-beam deposition of evaporated silver to provide reflective surfaces where necessary. The same fabrication process is used for both waveguides and microfluidic components of the chip and the final oxygen sensing device is shown in Figure 2. The oxygen sensors used for this experiment are created by a mixture of Platinum(II) octaethylporphine ketone (PtOEPK) [2] and polystyrene deposited on glass disks. This fluorescent dye has a maximum absorption at 592 nm and emits at 759 nm.
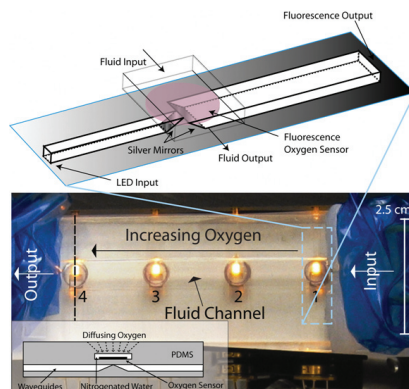
▲ Figure 2: A schematic of the integrated fluidic and photonic device showing the device and a cross sectional view. Fluorescence based oxygen sensors at the base of the fluidic channel lie on a plane sitting above the collection and excitation optics. A picture of the fabricated optical and fluidic integrated device is shown.

REFERENCES

[1] V.D. McGinniss, "Vaporous solvent treatment of thermoplastic substrates," United States Patent 4529563, 1985.
[2] D.B. Papkovsky, "Phosphorescent complexes of porphyrin ketones: Optical properties and application to oxygen sensing," *Anal. Chem.*, vol. 67, pp. 4112-4117, 1995.

# Nanoscale Thermal Imaging Microscopy of Thermoelectric Devices

P. Mayer, R.J. Ram
Sponsorship: ONR MURI

In many solids, a change in temperature produces a small change in the dielectric response of the material, and particularly in the index of refraction. By measuring the change in reflectance from a device or material whose temperature is modulated in some way, an image of the temperature change can be obtained, after proper calibration. This approach is useful for examining heat transport in electronic/optoelectronic devices since the heating due to a changing bias current or voltage can be measured. Unlike the case with typical (infrared) thermal imaging, deep sub-micron spatial resolution is possible. Shown below in Figure 1 are (uncalibrated) thermoreflectance images of the Joule and Peltier heating and cooling in a 4.9 μm-thick InGaAs-based superlattice incorporating semimetallic self-assembled ErAs nanodots, on an InP substrate. The ErAs dots and the superlattice both scatter phonons participating in cross-plane heat transport, reducing the thermal conductivity to below the alloy limit by nearly a factor of two. The dots and the superlattice are also expected to increase the free electron concentration, the electrical conductivity, and the Seebeck coefficient.

The thermal imaging technique used here relies on a CCD camera triggered 4 times per temperature cycle and averaged over many cycles, so that each pixel of the camera functions as a lock-in detector. Because the change in reflectance is small (e.g. 1 part in 10000, per degree Kelvin) it has been suggested that the temperature resolution of the technique is limited by the least significant bit size of the quantizer of the CCD array, giving rise to a minimum temperature resolution in the singe Kelvin range. However, due to the presence of noise in the pre-quantized signal, sufficient averaging can actually improve the resolution. We have demonstrated a temperature resolution on the order of 10 mK and developed a quantitative theory describing the statistics and accuracy of the measurement, set by the noise characteristics of the camera and the measurement characteristics. Figure 2 shows the measurement of a temperature signal smaller than that corresponding to the bit size of the CCD array, as a function of the measurement duration. The theoretically predicted mean and standard deviation are close to those measured.
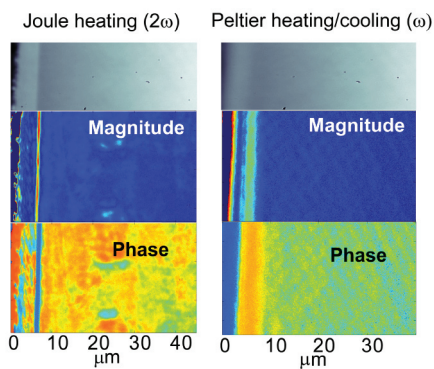
▲ Figure 1: Cross-plane magnitude and phase images of the Joule and Peltier contributions to the thermal response in a nanostructured thermoelectric element. Superlattice (clearly visible in the top photomicrographs) is to the left of the image.
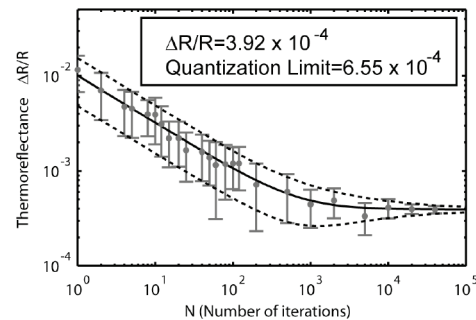
▲ Figure 2: Measurements (gray) and theoretical predictions (black) for sub-quantization thermoreflectance measurements. The measurement converges for sufficient iterations (long-enough duration).

Dynamic Range of Strained Ge-on-Silicon Photodiodes

J. Orcutt, R.J. Ram, O.L. Olubuyide, J.L. Hoyt
Sponsorship: DARPA

As photonic integrated circuits gain maturity in the silicon material system, new applications that require photonic components integrated with silicon electronic circuitry become possible. One such new application is the hybrid photonic-electronic analog-to-digital converter in which the sampling front-end is achieved optically and the digital conversion back-end is achieved electronically [1]. To allow this converter to achieve a high effective number of bits (ENOBs), an important figure-of-merit for these systems, photodetector with a high dynamic range that are compatible with an integrated CMOS platform are necessary. One such photodetector under development is a germanium-on-silicon photodiode that is CMOS-compatible. To characterize the linearity, we measured the spur-free dynamic range (SFDR) of the diodes using the test setup shown in Figure 1.

To calculate the SFDR, we measured the spectrum of the photodiode response to a two-tone RF-modulated input as a function of modulation amplitude. As shown in the microwave spectrum analyzer screen inset to Figure 1, third-order nonlinearities produce in-band intermodulation distortion products (IMD3) that limit the dynamic range of the detector. To ensure that observed nonlinearities are caused by the diodes, we examined the output of the link laser by using a ligh-twave front-end to the microwave spectrum analyzer and by replacing the Ge photodiodes with industry-standard Epitaxx InGaAs p-i-n photodiodes designed for CATV applications. To complete the data required to calculate SFDR, we measured the noise floor of the link, roughly integrating it over a 2-GHz bandwidth with the microwave spectrum analyzer. This data and the calculated SFDR are shown in Figure 2. The demonstrated 34-dB SFDR of this link would currently allow for 5.6 effective bits if it were the limiting factor in the converter's performance.
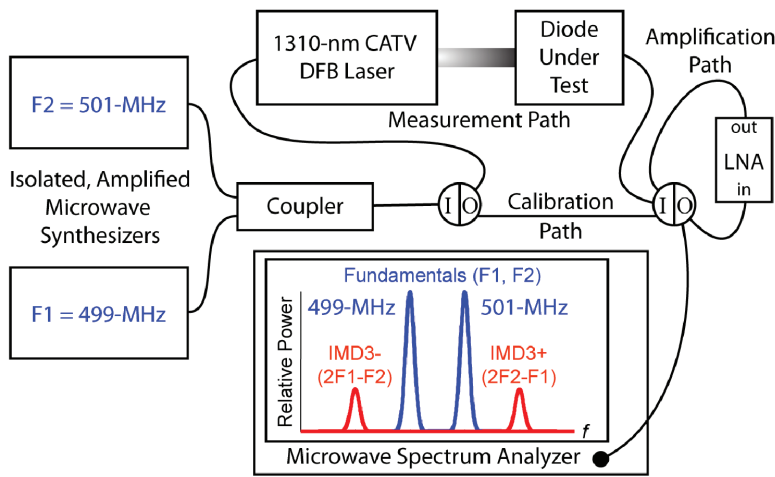
▲ Figure 1: Diagram showing the SFDR measurement setup. The I/0 blocks are microwave switches that enable switching between the measurement path and the calibration path, as well as the insertion of the optional amplification path. The block labeled "LNA" in the amplification path is a Miteq low-noise amplifier.
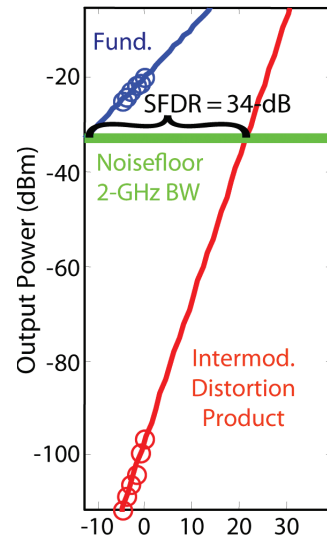
▲ Figure 2: Spur-free dynamic range measurement on a 100 x 100 µm Ge photodiode. The diode was biased at -3 V in this measurement.

REFERENCES

[1] F.X. Kärtner *et al.,* "Electronic photonic integrated circuits for high-speed, high-resolution, analog-to-digital conversion," *Proc. of SPIE*, vol. 6125, p. 612503, Mar. 2006.

Magnetic Oxide Films for Optical Isolators and Magneto-Electronic Devices

C.A. Ross, G.J. Dionne, M. Bolduc, A. Taussig, V. Sivakumar
Sponsorship: Lincoln Laboratory, ISN, MicroPhotonics Consortium

We have established a thin-film laboratory that includes a pulsed-laser deposition (PLD) system and an ultra-high vacuum sputter/analysis system. In PLD, a high-energy excimer laser is used to ablate a target, releasing a plume of material that deposits on a substrate to form a thin film. The PLD is particularly useful for making complex materials such as oxides because it preserves the stoichiometry of the target material.

We have been using PLD to deposit a variety of oxide films for magneto-optical devices such as isolators. These materials include iron oxide, which can adopt one of four different ferrimagnetic or antiferromagnetic structures depending on deposition conditions, and bismuth iron garnet (BIG, $Bi_3Fe_5O_{12}$), which is useful for magneto-optical isolators in photonic devices. The ideal material for an isolator combines high Faraday rotation with high optical transparency. Garnets have excellent properties but do not grow well on silicon substrates, making it difficult to integrate these materials. In contrast, iron oxide (maghemite) grows very well on MgO or Si, with high Faraday rotation but its optical absorption is high. Recently we have examined magnetic perovskite thin films such as Fe-doped barium titanate (Figure 1) [1] and Ce-doped orthoferrites (Figure 2). These materials show strong magneto-optical properties with weak optical absorption and the films grow with good quality onto MgO substrates. These films could be useful for waveguide isolators and other magneto-electronic devices in which optical absorption losses are critical. A second project involves the use of electrochemical methods to control the magnetization of iron oxide spinel structure films (magnetite or maghemite) grown on conducting substrates, making a chemically-switchable material. The insertion of Li ions by electrochemical discharge changes the oxidation state of the Fe(III) to Fe(II) and can reduce the magnetization of the film by about 30%, in a reversible process. Recent experiments on nanoparticles of iron oxide show much greater changes in magnetization, up to ~80%, indicating that the process is kinetically limited.
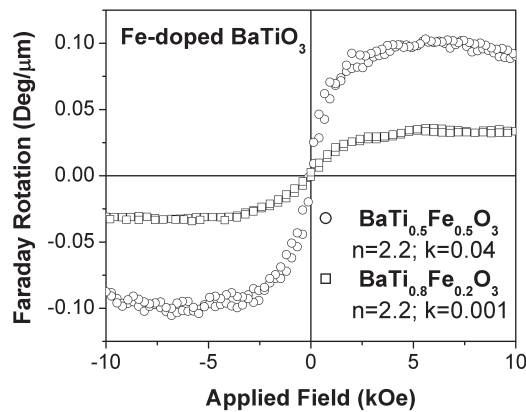
▲ Figure 1: Faraday rotation vs. applied field for 750-nm-thick $BaTi_{0.5}Fe_{0.5}O_3$ and $BaTi_{0.8}Fe_{0.2}O_3$ films grown in a vacuum on MgO substrates, with the field perpendicular to the film.
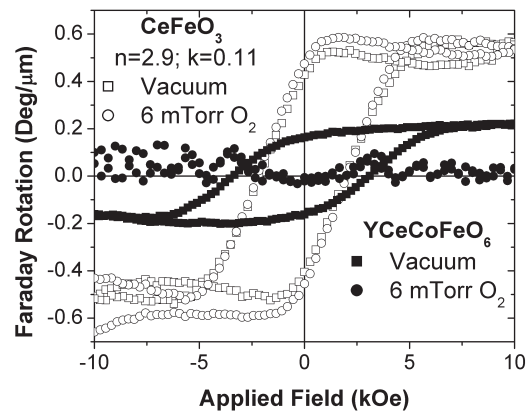
▲ Figure 2: Faraday rotation vs. applied field for 500-nm-thick $CeFeO_3$ and $YCeCoFeO_6$ films grown in a vacuum or under 6-mTorr O_2 pressure on MgO substrates, with the field perpendicular to the film.

REFERENCES

[1] A. Rajamani, G.F. Dionne, D. Bono, and C.A. Ross, "Faraday rotation, ferromagnetism, and optical properties in Fe-doped BaTiO$_3$," *J. App. Phys.*, vol. 98, no. 6, pp. 063907:1-4, Sept. 2005.

Characterization of Organic Field-effect Transistors for OLED Displays

K. Ryu, I. Kymissis, V. Bulovic, A.I. Akinwande, C.G. Sodini
Sponsorship: MARCO C2S2

Organic field-effect transistors (OFETs) provide exciting new applications because they can be made using low-temperature processing techniques such as thermal evaporation and solution-based patterning. The low-temperature processing enables the transistors to be fabricated on durable plastic substrates, which can be both flexible and very large. The solution-based patterning enables "printing" circuits like newspapers using a roll-to-roll method and can drive down cost. In addition, the fabrication process of OFETs is compatible with that of a variety of organic optoelectronics and sensors. Various sensor arrays such as pressure sensors, light sensors, and chemical sensors have been made successfully using OFETs [1-3]. One crucial area that needs to be researched in this field is how the different charge transport mechanisms and material sets in organic transistors change the design considerations in circuit applications compared to the traditional silicon MOSFETs. In this research, an optical-feedback organic LED (OLED) display is designed and fabricated in order to investigate this problem.

The contact resistance, threshold voltage, and mobility are extracted from top-contact and bottom-contact transistors with current-voltage (I-V), and capacitance-voltage (C-V) measurements. Extraction of contact resistance is found to be crucial in characterization of bottom-contact transistors as it obscures mobility extraction. Figures 1 and 2 show mobility extracted from various length transistors without and with taking contact resistance into consideration, respectively. In addition, mobility is found to increase as gate voltage increases contrary to the mobility dependence in crystal silicon MOSFETs where mobility decreases as gate voltage increases. Currently, slow transients, a manifestation of the trap-limited hopping transport in organic semiconductors, are being characterized.

Future work will focus on modeling transistors and simulating two main OFET components in the display, which are the switch and the transconductance amplifier.
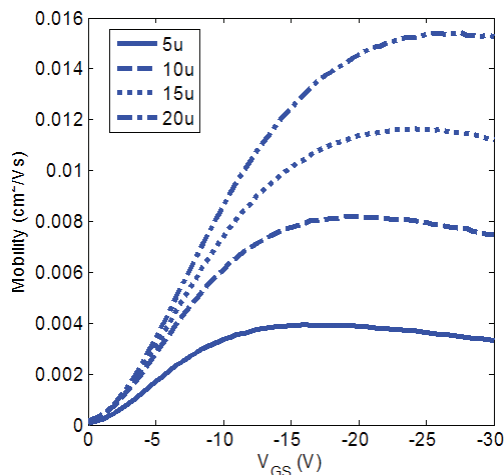
▲ Figure 1: Mobility extracted without taking contact resistance into consideration. The mobility decreases as the channel length shortens because effect of the contact resistance becomes more prevalent as the channel length shortens.
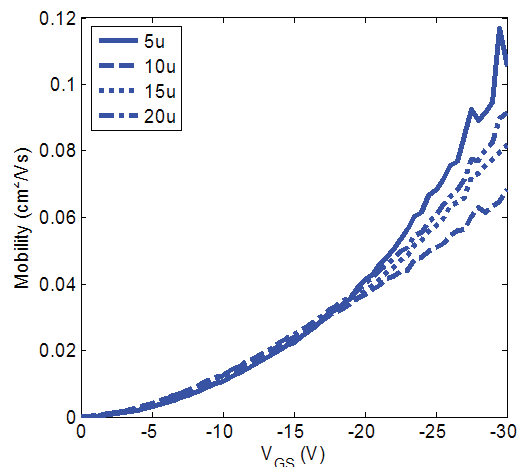
▲ Figure 2: Mobility extracted with contact resistance taken into consideration. The mobility is consistent from shorter to longer channel length.

REFERENCES

[1] T. Someya, H. Kawaguchi, and T. Sakurai, "Cut-and-paste organic FET customized ICs for application to artificial skin," *IEEE Int'l. Solid-State Circuits Conf. Dig. of Technical Papers*, Feb. 2004, pp. 288-289.

[2] H. Kawaguchi, S. Iba, Y. Kato, T. Sekitani, T. Someya, and T. Sakurai, "A sheet-type scanner based on a 3D stacked organic-transistor circuit with double word-line and double bit-line structure," *IEEE Int'l. Solid-State Circuits Conf. Dig. of Technical Papers*, Feb. 2005, pp. 580-581.

[3] V. Subramanian *et al.*, "Printed electronic nose vapor-sensors for consumer-product monitoring," *IEEE Int'l. Solid-State Circuits Conf. Digest of Technical Papers*, Feb. 2006, pp. 274-275.